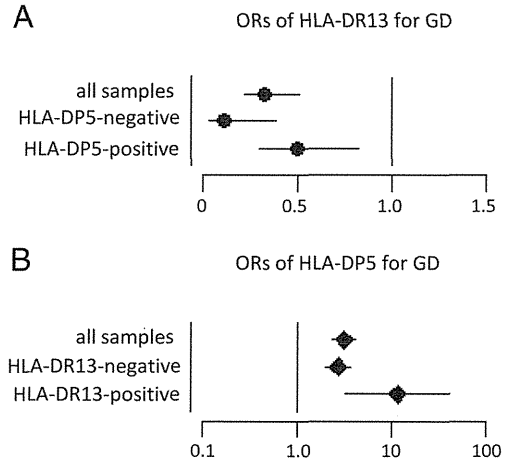

group	Number of individuals (DR13 positive/negative)	
	GD	control
all samples	33/514	78/403
DP5-negative	3/94	42/153
DP5-positive	30/420	36/250

group	Number of individuals (DP5 positive/negative)	
	GD	control
all samples	450/97	286/195
DR13-negative	420/94	250/153
DR13-positive	30/3	36/42

Figure 1. Effect size of susceptible or protective HLA antigens for the development of GD in the presence of protective or susceptible antigens. A, ORs of the protective antigen HLA-DR13 for GD in all patients (547 GD and 481 control), susceptible antigen HLA-DP5–negative patients (97 GD and 195 control), and HLA-DP5–positive patients (450 GD and 286 control). B, ORs of HLA-DP5 for GD in all patients, HLA-DR13–negative patients (514 GD and 403 control), and HLA-DR13-positive patients (33 GD and 78 control).

observation indicated that HLA-DR13 was epistatic to HLA-DP5 and more strongly epistatic to non-HLA-DP5–susceptible antigens in controlling GD development. Next, we divided patients into HLA-DR13–positive and –negative groups. Interestingly, the OR of HLA-DP5 was increased in the HLA-DR13–positive group compared with the OR in the HLA-DR13–negative group; the ORs of HLA-DP5 were 11.7 (95% CI = 3.28–41.44, $P = 1.5 \times 10^{-4}$) and 2.73 (95% CI = 2.02–3.69, $P = 5.6 \times 10^{-11}$) in the HLA-DR13–positive and –negative GD groups, respectively (Figure 1B). In HT, HLA-DR13 also had a strong protective effect against HT development in the HLA-A2–negative HT patient group (OR = 0.29, 95% CI = 0.17–0.48, $P = 5.2 \times 10^{-7}$) but not significantly in the HLA-A2–positive HT patient group (OR = 0.11, 95% CI = 0.01–1.09, $P = .096$). In contrast with GD, we concluded that significant epistasis was not observed between *HLA-DRB1*13:02* and *HLA-A*02:07* in HT.

Discussion

Among dozens of reported alleles (8–17), we clearly identified and confirmed 4 and 2 susceptible HLA molecules primarily associated with GD and HT, respectively, *HLA-B*35:01*, *HLA-B*46:01*, *HLA-DRB1*14:03*, and *HLA-DPB1*05:01* for GD and *HLA-A*02:07* and *HLA-DRB4* for HT. On the other hand, we concluded that the HLA-DR15 on HP1, HP-2, and HP-3 for GD and HP-2 for HT contribute to protecting against the development of the diseases. In a direct comparison between GD and HT, the frequencies of HLA-DR14 and HLA-DP5 were significantly higher in GD than in HT. Thus, we could clearly identify HLA molecules that distinguish GD from HT.

Because HLA-DP5 and HLA-DR14 are class II molecules, the unique immunological features of GD, including the production of agonistic antithyroid–stimulating hormone receptor autoantibodies, may be explained by the function of susceptible HLA-DP5 and HLA-DR14 in GD. In contrast, the susceptibilities controlled by HLA-A2, HLA-B46, HLA-B35, and HLA-DR53 are shared by GD and HT, suggesting that these HLA molecules might be responsible for the development of the common basic features of GD and HT as an AITD.

Furthermore, through the analysis of the epistatic interaction between protective and susceptible alleles, we could show that HLA-DR13 is epistatic to HLA-DP5, but not completely, in controlling the development of GD and that the blocking effect of HLA-DR13 on the second, third, and other susceptible *HLA* alleles is stronger than that on HLA-DP5. Furthermore, the OR of HLA-DP5 in the absence of HLA-DR13 was 2.73 (95% CI = 2.02–3.69), but to our surprise, it increased to 11.7 (95% CI = 3.28–41.44) in the presence of HLA-DR13, suggesting that the presence of HLA-DP5 is critical for the development of GD in the presence of resistant HLA-DR13 because the susceptibility conferred by non-DP-5 antigens is easily blocked by HLA-DR13.

How protective and susceptible HLA antigens play roles in the regulation of autoimmune response in the diseases is still an enigma. To explain the protective effect of HLA antigens on the development of GD and HT, although we could not exclude a breakdown in central tolerance, the possibility that protective HLA molecules induce immunosuppressive T cells, such as regulatory T cells (20), exist. Thus, the elucidation of HLA molecules controlling the susceptibilities and resistance to GD and HT in this study provides a genetic and molecular basis for future

The Endocrine Society. Downloaded from press.endocrine.org by [${individualUser.displayName}] on 10 March 2015. at 00:36 For personal use only. No other uses without permission. . All rights reserved.

analysis of autoimmune response at a cellular level in these diseases.

Acknowledgments

We thank all of the participants for providing blood samples.

Address all correspondence and requests for reprints to: Takehiko Sasazuki, MD, PhD, Institute for Advanced Study, Kyushu University, 3-1-1 Maidashi, Higashi-ku, Fukuoka 812-8582, Japan. E-mail: sasazuki@bioreg.kyushu-u.ac.jp.

This work was supported by KAKENHI (22133009) from the Ministry of Education, Culture, Sports, Science and Technology, Japan.

Disclosure Summary: The authors have nothing to disclose.

References

1. **Tunbridge WM, Evered DC, Hall R, et al.** The spectrum of thyroid disease in a community: the Whickham survey. *Clin Endocrinol (Oxf).* 1977;7:481–493.
2. **Jacobson DL, Gange SJ, Rose NR, Graham NM.** Epidemiology and estimated population burden of selected autoimmune diseases in the United States. *Clin Immunol Immunopathol.* 1997;84:223–243.
3. **Weetman AP.** Autoimmune thyroid disease. *Autoimmunity.* 2004; 37:337–340.
4. **Eschler DC, Hasham A, Tomer Y.** Cutting edge: The etiology of autoimmune thyroid diseases. *Clin Rev Allergy Immunol.* 2011;41: 190–197.
5. **Brix TH, Kyvik KO, Christensen K, Hegedüs L.** Evidence for a major role of heredity in Graves' disease: a population-based study of two Danish twin cohorts. *J Clin Endocrinol Metab.* 2001;86:930–934.
6. **Wellcome Trust Case Control Consortium, Australo-Anglo-American Spondylitis Consortium (TASC), et al.** Association scan of 14,500 nonsynonymous SNPs in four diseases identifies autoimmunity variants. *Nat Genet.* 2007;39:1329–1337.
7. **Nakabayashi K, Tajima A, Yamamoto K, et al.** Identification of independent risk loci for Graves' disease within the MHC in the Japanese population. *J Hum Genet.* 2011;56:772–778.
8. **Zeitlin AA, Heward JM, Newby PR, et al.** Analysis of HLA class II genes in Hashimoto's thyroiditis reveals differences compared to graves' disease. *Genes Immun.* 2008;9:358–363.
9. **Simmonds MJ, Howson JM, Heward JM, et al.** Regression mapping of association between the human leukocyte antigen region and Graves disease. *Am J Hum Genet.* 2005;76:157–163.
10. **Chen QY, Huang W, She JX, et al.** HLA-DRB1*08, DRB1*03/DRB3*0101, and DRB3*0202 are susceptibility genes for Graves' disease in north American Caucasians, whereas DRB1*07 is protective. *J Clin Endocrinol Metab.* 1999;84:3182–3186.
11. **Kawa A, Nakamura S, Nakazawa M, et al.** HLA-BW35 and B5 in Japanese patients with Graves' disease. *Acta Endocrinol (Copenh).* 1977;86:754–757,
12. **Dong RP, Kimura A, Okubo R, et al.** HLA-A and DPB1 loci confer susceptibility to Graves' disease. *Hum Immunol.* 1992;35:165–172.
13. **Katsuren E, Awata T, Matsumoto C, Yamamoto K.** HLA class II alleles in Japanese patients with Graves' disease: weak associations of HLA-DR and -DQ. *Endocr J.* 1994;41:599–603.
14. **Takahashi M, Yasunami M, Kubota S, Tamai H, Kimura A.** HLA-DPB1*0202 is associated with a predictor of good prognosis of Graves' disease in the Japanese. *Hum Immunol.* 2006;67:47–52.
15. **Park MH, Park YJ, Song EY, et al.** Association of HLA-DR and -DQ genes with Graves disease in Koreans. *Hum Immunol.* 2005;66:741–747.
16. **Wan XL, Kimura A, Dong RP, Honda K, Tamai H, Sasazuki T.** HLA-A and -DRB4 genes in controlling the susceptibility to Hashimoto's thyroiditis. *Hum Immunol.* 1995;42:131–136.
17. **Katahira M, Hanakita M, Ito T, Suzuki M.** Effect of human leukocyte antigen class II genes on Hashimoto's thyroiditis requiring replacement therapy with levothyroxine in the Japanese population. *Hum Immunol.* 2013;74:607–609.
18. **Purcell S, Neale B, Todd-Brown K, et al.** PLINK: a tool set for whole-genome association and population-based linkage analyses. *Am J Hum Genet.* 2007;81:559–575.
19. **Barrett JC, Fry B, Maller J, Daly MJ.** Haploview: Analysis and visualization of LD and haplotype maps. *Bioinformatics.* 2005;21: 263–265.
20. **Sakaguchi S, Yamaguchi T, Nomura T, Ono M.** Regulatory T cells and immune tolerance. *Cell.* 2008;133:775–787.

The Endocrine Society. Downloaded from press.endocrine.org by [${individualUser.displayName}] on 10 March 2015. at 00:36 For personal use only. No other uses without permission. . All rights reserved.

ORIGINAL ARTICLE

JBMR®

A Recurrent De Novo *FAM111A* Mutation Causes Kenny–Caffey Syndrome Type 2

Tsuyoshi Isojima,[1] Koichiro Doi,[2] Jun Mitsui,[3] Yoichiro Oda,[4] Etsuro Tokuhiro,[5] Akihiro Yasoda,[6] Tohru Yorifuji,[7] Reiko Horikawa,[8] Jun Yoshimura,[2] Hiroyuki Ishiura,[3] Shinichi Morishita,[2] Shoji Tsuji,[3] and Sachiko Kitanaka[1]

[1]Department of Pediatrics, Graduate School of Medicine, The University of Tokyo, Tokyo, Japan
[2]Department of Computational Biology, Graduate School of Frontier Sciences, The University of Tokyo, Kashiwa, Japan
[3]Department of Neurology, Graduate School of Medicine, The University of Tokyo, Tokyo, Japan
[4]Department of Pediatrics, Ohta Nishinouchi Hospital, Koriyama, Japan
[5]Department of Pediatrics, Odawara City Hospital, Odawara, Japan
[6]Department of Medicine and Clinical Science, Kyoto University Graduate School of Medicine, Kyoto, Japan
[7]Department of Pediatric Endocrinology and Metabolism, Children's Medical Center, Osaka City General Hospital, Osaka, Japan
[8]Division of Endocrinology and Metabolism, National Center for Child Health and Development, Tokyo, Japan

ABSTRACT

Kenny–Caffey syndrome (KCS) is a rare dysmorphologic syndrome characterized by proportionate short stature, cortical thickening and medullary stenosis of tubular bones, delayed closure of anterior fontanelle, eye abnormalities, and hypoparathyroidism. The autosomal dominant form of KCS (KCS type 2 [KCS2]) is distinguished from the autosomal recessive form of KCS (KCS type 1 [KCS1]), which is caused by mutations of the tubulin-folding cofactor E (*TBCE*) gene, by the absence of mental retardation. In this study, we recruited four unrelated Japanese patients with typical sporadic KCS2, and performed exome sequencing in three patients and their parents to elucidate the molecular basis of KCS2. The possible candidate genes were explored by a de novo mutation detection method. A single gene, *FAM111A* (NM_001142519.1), was shared among three families. An identical missense mutation, R569H, was heterozygously detected in all three patients but not in the unaffected family members. This mutation was also found in an additional unrelated patient. These findings are in accordance with those of a recent independent report by a Swiss group that KCS2 is caused by a de novo mutation of *FAM111A*, and R569H is a hot spot mutation for KCS2. Although the function of FAM111A is not known, this study would provide evidence that FAM111A is a key molecule for normal bone development, height gain, and parathyroid hormone development and/or regulation. © 2014 American Society for Bone and Mineral Research.

KEY WORDS: KENNY–CAFFEY SYNDROME; *FAM111A*; PARATHYROID-RELATED DISORDERS; HYPOMAGNESEMIA

Introduction

Kenny–Caffey syndrome (KCS) (OMIM #244460, %127000) is a rare dysmorphologic syndrome characterized by severe proportionate short stature with adult heights of 121 to 149 cm, cortical thickening and medullary stenosis of tubular bones, delayed closure of the anterior fontanelle, eye abnormalities, and hypocalcemia owing to hypoparathyroidism.[1–4] KCS is classified into two types according to its clinical features and inheritance pattern. Classical cases have normal intelligence and are transmitted as an autosomal dominant trait or sporadically and are called KCS type 2 (KCS2) (OMIM %127000).[5] Cases having mental and prenatal growth retardation and transmitted as an autosomal recessive trait are called KCS type 1 (KCS1) (OMIM #244460).[4,6,7]

In 2002, a study of 65 individuals from 34 pedigrees of Middle Eastern origin resulted in the identification of mutations of the tubulin-folding cofactor E (*TBCE*) gene as the cause of KCS1. *TBCE* encodes a molecular chaperone required for heterodimerization of α-tubulin with β-tubulin.[8] KCS2 is extremely rare, with only 5 sporadic cases reported in Japan.[9–12] Because of this rarity, the cause of KCS2 has been unknown until it was recently reported to involve the "family with sequence similarity 111, member A" (*FAM111A*) gene (NM_001142519.1) by a Swiss group in 2013.[13]

In this study, we recruited 4 Japanese patients with typical sporadic KCS2 having normal intelligence and performed whole exome sequencing in 3 unrelated trios to elucidate the molecular basis of KCS2. We hypothesized that KCS2 is caused by de novo mutations and built a de novo mutation detection pipeline to

Received in original form June 10, 2013; revised form August 21, 2013; accepted August 27, 2013. Accepted manuscript online August 31, 2013.
Address correspondence to: Sachiko Kitanaka, MD, PhD, Department of Pediatrics, Graduate School of Medicine, The University of Tokyo, 7-3-1 Hongo, Bunkyo-ku, Tokyo, 113-8655, Japan. E-mail: sachi-tky@umin.ac.jp
Additional Supporting Information may be found in the online version of this article.

Journal of Bone and Mineral Research, Vol. 29, No. 4, April 2014, pp 992–998
DOI: 10.1002/jbmr.2091
© 2014 American Society for Bone and Mineral Research

process the raw data from exome sequencing. Using this method, we found an identical de novo mutation in *FAM111A* in all 4 patients. This and the reported independent studies provide evidence that *FAM111A* is the cause of KCS2, and R569H is a hot spot mutation for KCS2.

Materials and Methods

Subjects

Case 1

This 10-year-old girl (Fig. 1, I-1)[9] was born at 40 weeks of gestation to nonconsanguineous, healthy Japanese parents. Polysyndactyly was noticed at birth. At 3 months of age, she was referred to a pediatric endocrinologist because of growth retardation. Her body length, body weight, and head circumferences were 55 cm (−2.5 SD), 5092 g (−1.8 SD), and 37.3 cm (0.2 SD), respectively. She was found to have liver dysfunction with a serum aspartate aminotransferase (AST) level of 227 U/L (reference range 21 to 75) and serum alanine aminotransferase (ALT) level of 227 U/l (reference range 11 to 69). Basal serum insulin-like growth factor (IGF-I), calcium (Ca), and phosphorus (P) levels were within normal limits. At the age of 1 year, hypocalcemia was revealed. Her serum Ca, P, and intact parathyroid hormone (PTH) levels were 1.6 mmol/L (reference range 2.1 to 2.4), 2.6 mmol/L (reference range 0.88 to 1.4), and 11 ng/L (reference range 15 to 50), respectively, with a normal magnesium (Mg) level of 0.86 mmol/L (reference range 0.74 to 0.90). Her serum $1,25(OH)_2D$ level, serum alkaline phosphatase level, and urine Ca/creatinine ratio were within normal ranges. Brain computed tomography (CT) revealed calcification in the basal ganglia (Fig. 2*A*). She was diagnosed with primary hypoparathyroidism and was treated with alfacalcidol [$1\alpha(OH)D_3$]. At 2 years of age, she was diagnosed with KCS2 based on clinical manifestations of proportionate short stature, cortical thickening and medullary stenosis confirmed by radioscopic study (Fig. 2*B*), macrocephaly with delayed closure of the anterior fontanelle, eye abnormalities (hypermetropia and pseudopapilledema), and normal intelligence. Magnesium oxide was administered because of a low serum Mg level (below 0.62 mmol/L) at 3 years of age.

Case 2

This 16-year-old boy (Fig. 1, II-4)[10] was born at 41 weeks of gestation to nonconsanguineous, healthy Japanese parents. When he was 23 days old, he had a generalized convulsion because of hypocalcemia. At this time, his serum Ca, P, Mg, and intact PTH levels were 1.5 mmol/L, 3.1 mmol/L, 0.74 mmol/L, and undetectable, respectively. T-cell subset was normal. He was treated with alfacalcidol on the basis of a diagnosis of primary hypoparathyroidism. Magnesium sulfate was added because of his low serum Mg level at the age of 1 year. He suffered repeated bouts of acute otitis media until the age of two years. His serum IgG level was within the normal range. At 3 years and 1 month, his height, weight, and head circumference were 77.9 cm (−4.4 SD), 9.9 kg (−2.7 SD), and 47.4 cm (−1.5 SD), respectively. He had normal intelligence for his age. He was diagnosed with KCS2 based on clinical findings of proportionate short stature, medullary stenosis revealed by radiography, a widely open anterior fontanelle (Fig. 2*C*, skull radiograph at 9 years), and hypermetropia. He also suffered severe atopic dermatitis after normalization of his serum Ca levels. His growth chart is shown in Fig. 2*D*.

Case 3

This 22-year-old woman (Fig. 1, III-9)[11] was born at 40 weeks of gestation to nonconsanguineous, healthy Japanese parents following an uneventful pregnancy. At 1 month, she had an episode of generalized convulsions because of hypocalcemia. At this episode, her serum Ca, P, Mg, and intact PTH levels were 1.3 mmol/L, 2.9 mmol/L, 0.49 mmol/L, and undetectable, respectively. Oral alfacalcidol administration was started on the basis of a diagnosis of primary hypoparathyroidism. At the age of 5 years 1 month, she was referred to another hospital. Her height was 84.2 cm (−5.3 SD), and her weight was 12.2 kg (−2.2 SD). She had normal intelligence. Brain CT revealed fine calcification in the basal ganglia. Based on clinical manifestations of proportionate short stature, medullary stenosis of the long bones typical of KCS, a 1 × 1-cm opening of her anterior fontanelle, normal intelligence, and hypermetropia, she was diagnosed with KCS2. The patient was started with a combination therapy of vitamin D and magnesium sulphate. Fig. 2*E* shows her radiograph at 14 years of age.

Case 4

This 38-year-old man (Fig. 1, IV-13)[12] was born at 40 weeks of gestation to nonconsanguineous, healthy Japanese parents following an uneventful pregnancy. At 8 days of age, he had a generalized convulsion, and hypocalcemia (0.75 mmol/L) and hypomagnesemia (0.18 mmol/L) were detected. The convulsion was controlled by intravenous administration of Ca gluconate and magnesium sulfate until he was 15 days old. At 4 years of age, he again had an episode of generalized convulsion because of hypocalcemia. At this episode, his serum Ca, P, and intact PTH levels were 1.2 mmol/L, 2.6 mmol/L, and undetectable, respectively. He was diagnosed with primary hypoparathyroidism, and oral alfacalcidol and Ca lactate administration were started. He suffered repeated acute otitis media during infancy and was affected with empyema and bacterial meningitis at 4 years of age. Hypogammaglobulinemia was found, and he was administered gamma globulin intermittently. At 12 years of age, he was referred to another hospital for further investigation. His height was 99 cm (−6.3 SD), and his weight was 16.2 kg (−3.3 SD). He had normal intelligence with an intelligence quotient score of 105. Brain CT revealed fine calcification in the basal ganglia. Based on clinical manifestations of proportionate short stature, medullary stenosis of the long bones, a 4.2 × 1.8-cm opening of his anterior fontanelle, and eye abnormalities (hypermetropia, amblyopia, and pseudopapilledema), he was diagnosed with KCS2. Mg loading and Ca restriction tests revealed that his hypoparathyroidism was secondary to hypomagnesemia. The patient was then changed from vitamin D and Ca lactate to magnesium sulfate treatment, which successfully corrected his serum Ca levels.

We recruited these 4 Japanese patients with clinically diagnosed typical sporadic KCS2 (Fig. 1). Supplemental Table S1{TBL S1} summarizes the clinical characteristics of the 4 patients. We obtained peripheral blood samples from all 4 patients, together with those of 9 unaffected parents or siblings, with informed consent for DNA analysis (Fig. 1). The study was performed with the approval of the Ethics Committee of The University of Tokyo and of each institution where the samples

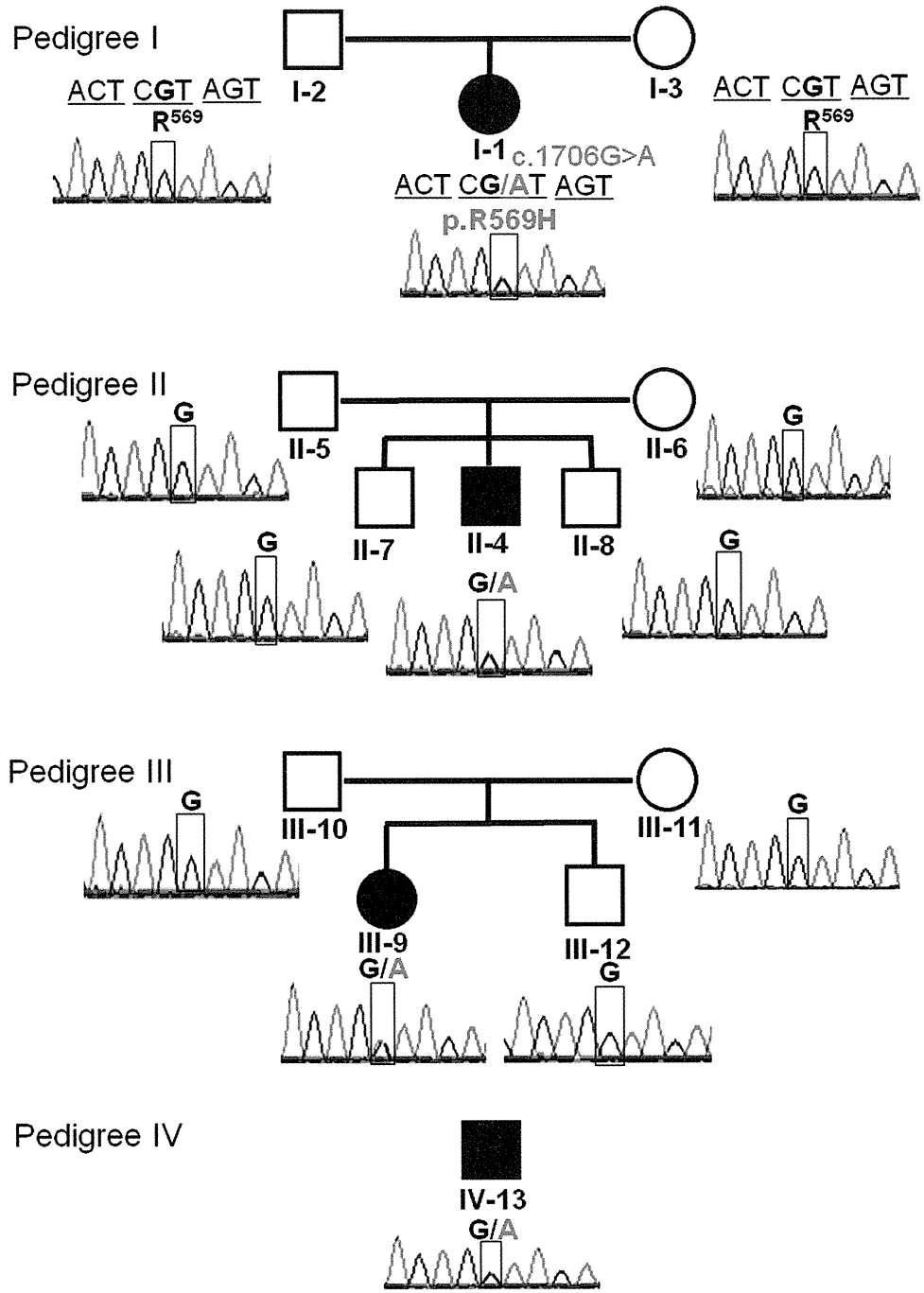

Fig. 1. Four pedigrees analyzed in this study, showing the chromatograms of Sanger sequencing reactions of the *FAM111A* mutation in patients and family members. Data were obtained by Sanger sequencing during the confirmation process. All mutations were checked by bidirectional sequencing. In each pedigree, a black symbol represents the proband, a square indicates a male, and a circle shows a female. In the chromatogram, black letters indicate the wild-type nucleotide sequence. Nucleotides in red indicate mutations. R569H was identified in all probands but not in any of the unaffected family members.

were collected, and conducted in accordance with the Declaration of Helsinki. Genomic DNA was extracted from peripheral white blood cells of the patients and family members using a QIAamp DNA Blood Midi Kit (Qiagen, Hilden, Germany). Healthy Japanese volunteers were recruited, and DNA was extracted with informed consent.

Exome sequencing

Exome sequences were enriched using a TruSeq Exome Enrichment Kit (Illumina, San Diego, CA, USA) from 1 μg of genomic DNA, according to the manufacturer's instructions. The captured DNA samples were subjected to massively parallel

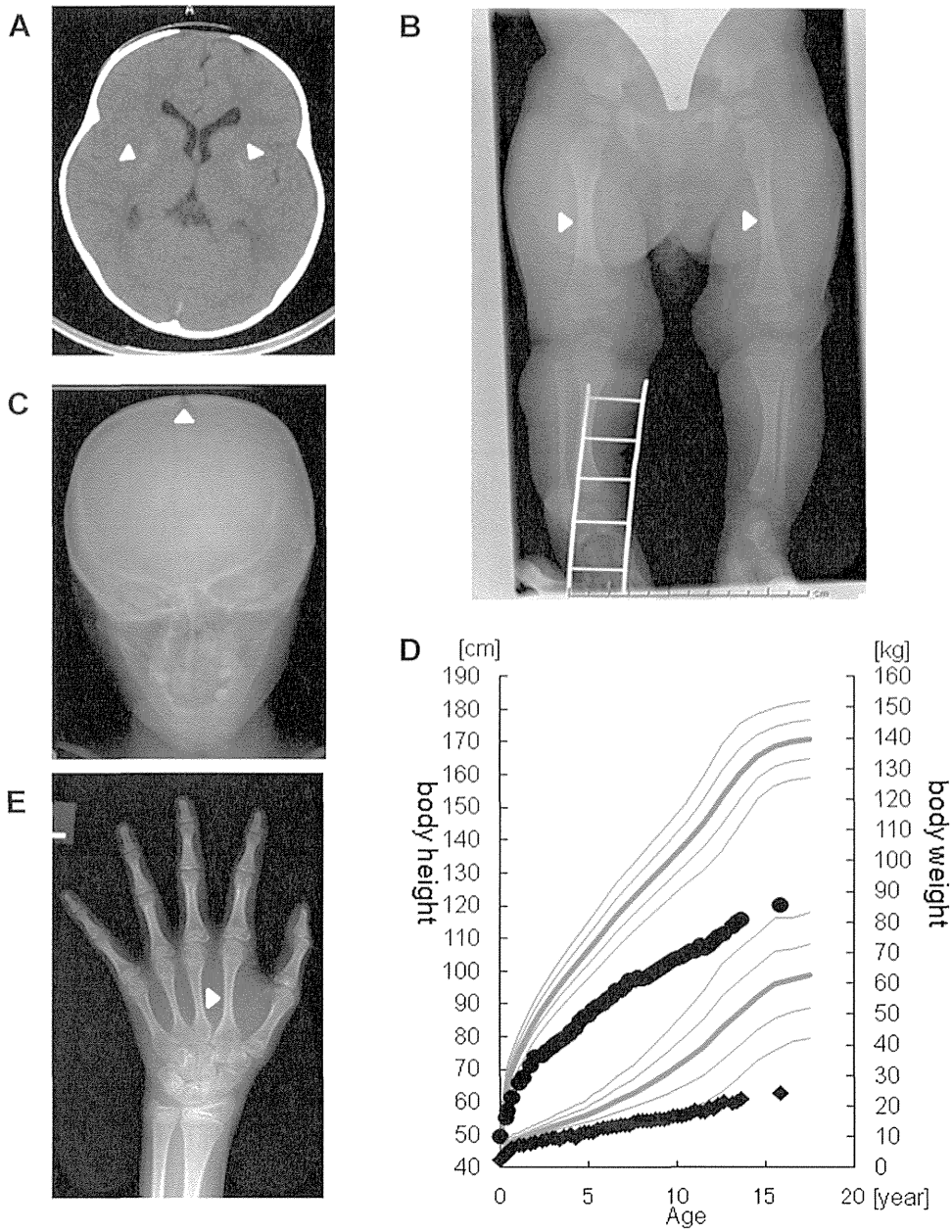

Fig. 2. Radiographic studies and growth charts of probands. (*A*) Brain computed tomography of patient I-1. The arrowheads indicate calcification in the basal ganglia. (*B*) Radiograph of patient I-1 at diagnosis. Cortical thickening and medullary stenosis are evident. The object shown in the right leg is used for fixing a peripheral catheter. (*C*) Radiograph of patient II-4 at age 9 years. It is of note that the anterior fontanelle is open. (*D*) Growth chart of patient II-4 superimposed on the standard growth chart for a Japanese boy. Black circles indicate the patient's height, and black squares indicate his weight. (*E*) Radiograph of patient III-9. Cortical thickening and medullary stenosis can be observed.

sequencing (100-bp paired-end reads) on an Illumina HiSeq2000 sequencing system (Illumina). An average of 95 million reads of the sequence data was obtained for each individual. On an average, 98.50% of the total bases were mapped to the reference genome with a mean coverage of 140.5 ×, which encompassed 91.94% of the targeted regions with coverage >10× (Supplemental Table S2).{TBL S2} The Burrows-Wheeler Aligner (BWA) package[14] and SAMtools[15] were used as default settings for alignment of raw reads and detection of single-nucleotide variants (SNVs) and indels. Subsequently, SNVs and indels were filtered with three trio samples (ie, pedigrees I, II, and III) (Supplemental Fig. S1). We extracted both homo/heterozygous nonsynonymous coding variants, which were called in the proband, and filtered these candidates using the following three steps:

Step 1: Using candidate de novo mutations that are homozygous references in both parents and are supported by 10 or more high-quality reads at the mutated sites for every trio member.

Step 2: Using reliable homozygous references in each parent such that the likelihood of heterozygosis, ${}_nC_i\,(1/2)^i\,(1/2)^{n-i}$, is less than that of homozygosis, ${}_nC_i\,(999/1000)^i(1/1000)^{n-i}$, where the average error rate is assumed to be 1/1000, n represents the number of total reads, and i is the number of reads consistent with the reference. One may have an impression that this condition does not often hold true; however, we often observed cases that violated this condition, especially when the reference base was mutated into one of the other three bases with an almost equal probability.

Step 3: Using reliable de novo mutations of the proband such that the number of alternative allele reads was at least 30% among the total reads, which is the condition proposed in a recent report.[16]

Sanger sequencing

Sanger sequencing was performed to detect *TBCE* (KCS1) and validate the presence of each variant detected by exome sequencing in patients with KCS2 and the absence of each in the genomes of the parents and siblings. The entire coding region and exon–intron boundaries of *TBCE* and *FAM111A* were amplified from genomic DNA by polymerase chain reaction (PCR) using the designed PCR primers (Supplemental Table S3). {TBL S3} Subsequently, PCR products were sequenced using an ABI Prism BigDye Terminator Cycle Sequencing Ready Reaction Kit (PE Applied Biosystems, Foster City, CA, USA) and the forward and reverse primers used for PCR amplification. Direct sequencing in both directions was performed on an autosequencer (PE Applied Biosystems 3130 × 1, Genetic Analyzer).

FAM111A mRNA expression analysis

Total RNA was prepared using ISOGEN reagent (Nippon Gene, Osaka, Japan), according to the manufacturer's instructions, from peripheral white blood cells of the patients and family members. Total RNA (4 μg) was used to synthesize cDNA with the SuperScript Preamplification System for first-strand cDNA synthesis (Life Technologies, Rockville, MD, USA). mRNA levels were measured using an ECO real-time PCR system (Illumina) and KAPA SYBR Fast qPCR Kit (Kapa Biosystems, Woburn, MA, USA) using the following primer pairs: FAM111Ae5-2F and FAM111Ae5-2R; FAM111Ae5-3F and 5′-CCTCATCACTCATCATTTCTACATCC-3′; GAPDH, 5′-GAAGGTGAAGGTCGGAGTC-3′ (F) and 5′-GAAGATGGTGATGGGATTTC-3′ (R). The relative mRNA level was calculated using an arithmetic formula based on the difference between the threshold cycle of a given target cDNA and that of an endogenous reference cDNA. Direct sequencing of the RT-PCR products was performed by Sanger sequencing as for DNA samples.

Results

We first confirmed by Sanger sequencing that none of the 4 patients had *TBCE* mutations. This finding, together with the fact that all the patients were of normal intelligence, distinguishes these patients from patients with KCS1.

We hypothesized that these sporadic cases may be caused by de novo mutations in novel nonsynonymous coding variants. Whole exome sequencing was performed for 3 patients (I-1, II-4, and III-9; Fig. 1) and their parents (I-2, I-3, II-5, II-6, III-10, and III-11; Fig. 1). Statistical data of exome sequencing experiments are shown in Supplemental Table S2. The candidate variants were selected according to the processes described in Materials and Methods based on the de novo mutation detection pipeline designed in the present study (Supplemental Fig. S1). Supplemental Table S4{TBL S4} summarizes the results of filtering to detect candidate genes for KCS2. To select variants as candidate mutations for KCS2, variations that caused amino acid substitution were extracted, which resulted in 11,024 (pedigree I), 10,828 (pedigree II), and 11,020 (pedigree III) SNVs and indels. After three filtering steps, 5 (pedigree I), 5 (pedigree II), and 6 (pedigree III) SNVs were identified. Among the candidate genes filtered using the three aforementioned filtering steps, only one single gene, *FAM111A* (NM_001142519.1), was shared among all 3 families. Sanger sequence analysis of all exons of *FAM111A* confirmed an identical c.1706G > A heterozygous mutation in exon 5 in all 3 patients (Fig. 1). This mutation is predicted to result in substitution of arginine to histidine in codon 569 (R569H). None of the unaffected family members had this mutation, indicating that R569H was a de novo mutation. This mutation was also found in an additional unrelated patient (IV-13).

R569H is not present in 373 Japanese healthy control subjects of an in-house exome database, and not in another 100 alleles from 50 unrelated healthy Japanese individuals by Sanger sequencing. It was also not found in the Japanese SNP control database established by the National Bioscience Data Base Center that has 1 million genome-wide SNPs of 700 samples (http://gwas.biosciencedbc.jp/snpdb/snp_top.php), nor among 6500 samples listed on the exome variant server (http://evs.gs.washington.edu/EVS/), implying that the minor allele frequency is less than 0.01% in these data. However, one SNP was found in the 1000 Genomes database at R569 (rs184251651), which results in substitution to "cysteine" (minor allele frequency 0.1%).

We assessed the functionality of the R569H mutation using the Sorting Intolerant From Tolerant (SIFT) (http://sift.jcvi.org) and Polymorphism Phenotyping 2 (PolyPhen2) (http://genetics.bwh.harvard.edu/pph2) tools, by homology modeling and threading. These in silico studies predicted R569H as "tolerated" and "benign," respectively.

We analyzed the expression levels of *FAM111A* mRNA in peripheral white blood cells by real-time PCR. *FAM111A* expression levels in the patients were comparable with those in unaffected family members and normal controls (data not shown). We also found that mutant and wild-type *FAM111A* were equivalently expressed in the patients, which were identified by sequencing the reverse-transcribed PCR products.

Discussion

In the present study, we identified *FAM111A* as the gene responsible for KCS2 by applying an exome sequencing strategy, and we identified a heterozygous identical de novo *FAM111A* mutation, R569H, in 4 Japanese patients with KCS2. While preparing this article, another independent research group from Switzerland reported similar findings following whole exome sequencing of the patients.[13] They reported that all 5 clinically diagnosed KCS2 patients had de novo *FAM111A* mutations. Most interestingly, 4 of the 5 patients from different countries had the same R569H mutation as detected in our patients. Our 4 pedigrees are unrelated to each other and live in different areas in Japan. Moreover, the parents of the 3 patients did not have the mutation, suggesting that this recurrent mutation was caused by sporadic mutation. Taken together, these two independent

studies confirm that *FAM111A* is the causative gene for KCS2, and R569H is the hot spot mutation of KCS2.

FAM111A encodes a previously uncharacterized protein consisting of 611 amino acids. The carboxy-terminal half of the protein has homology to trypsin-like peptidases, and the catalytic triad specific to such peptidases is conserved.[17] Transcriptional expression of *FAM111A* is ubiquitous according to the human protein atlas (http://www.proteinatlas.org/ENSG00000166801/normal). It is expressed in the parathyroid gland and bone, but the expression levels are similar to those in other tissues. FAM111A has 35% amino acid homology to FAM111B, a paralog located on 11q12.1 at a distance of only 16 kb from FAM111A. The functions of FAM111A and FAM111B are largely unknown. A recent report showed that FAM111A functions as a host range restriction factor and is required for viral replication and gene expression by specifically interacting with Simian Virus 40 large T antigen (LT).[17] In addition, *FAM111A* mRNA and protein levels have been shown to be regulated in a cell cycle-dependent manner with the lowest expression during the G0 or quiescent phase and peak expression during the G2/M phase.[17] Another recent report revealed that variants in the region including *FAM111A* and *FAM111B* were associated with prostate cancer.[18] However, the clinical course of disease in our 4 patients revealed neither increased viral infections nor carcinogenesis up to early adulthood.

In silico analyses suggested that the de novo mutation (R569H) would not significantly affect the function of FAM111A. We also found that the mutant *FAM111A* mRNA was expressed similarly to the wild type in peripheral blood cells. This raises the question of how this mutation causes KCS2. One hypothesis is that this mutation does not cause loss of function of the protein but rather modulates its peptidase activity for a particular target peptide in a mutant-specific way. Another possibility is that FAM111A functions with some physiological partner(s) and the disease occurs as a result of specific modulation of this putative network. This may fit the observation that FAM111A is regulated in a cell-dependent manner and interacts with the LT C-terminal region.[17] We speculate that one of the candidate partner proteins is TBCE because KCS1 and KCS2 share distinctive phenotypic features: skeletal dysmorphic features and primary hypoparathyroidism.

Some diseases are caused by specific mutations of a single gene. Some mutations may cause a gain-of-function effect, as in achondroplasia or McCune–Albright syndrome,[19,20] whereas others have an unknown function, as in Caffey syndrome caused by mutations in *COL1A1*[21] or in several diseases related to *FGFR3*. In this study, we found that a specific mutation (R569H) of *FAM111A* would lead to KCS2. Intriguingly, one SNP was found in the 1000 Genomes database at R569 (rs184251651), which results in substitution to "cysteine." This SNP has been reported to have minor allele frequency of 0.1% (only one allele) and is not validated. Moreover, the absence of the SNP in 6500 samples in the exome variant server suggests a possibility of sequencing error in the database. Nevertheless, it might be speculated that a specific change to "histidine" may lead to an unidentified function of this protein resulting in KCS2, which is not caused by other amino acids. This hypothesis will be supported by the fact that this amino acid is not well conserved among various species (Fig. 3).

It is reported that 95% and 97% of KCS1 cases had prenatal and postnatal growth retardation, and mental retardation, respectively.[22] In contrast, most of the reported KCS2 patients, including our patients with *FAM111A* mutations, had normal

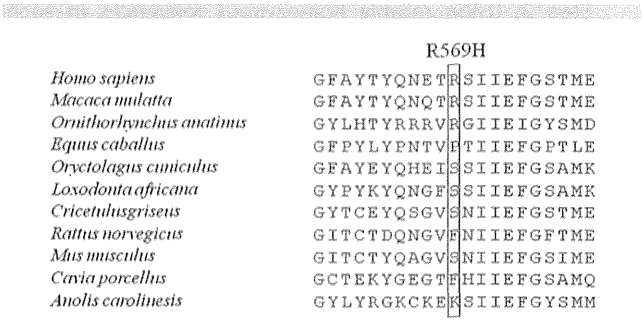

Fig. 3. Homologous comparison of the altered protein. Letters in the rectangular box indicate the human *FAM111A* R569 residue. It is of note that R569 is not well conserved among various species.

birth weight and length and normal intelligence (Supplemental Table S1).[13] These phenotypic differences between KCS1 and KCS2 suggest that the *FAM111A* mutation does not affect bone development and height gain in the fetus but becomes important postnatally. It also suggests that the *FAM111A* mutation does not affect mental development. Now that *FAM111A* has been identified as a causative gene for KCS2, further studies on the physiological function of FAM111A and TBCE should be performed to uncover the phenotypic differences between these two types.

There are several human diseases, as well as mouse models of hypoparathyroidism, caused by aberrations in the cascade of genes indispensable for the development and regulation of the parathyroid gland.[23,24] To date, FAM111A is not known to relate to any of these genes. There have been only a few reports describing the pathophysiology of hypoparathyroidism in KCS. Absence of the parathyroid glands has been reported in some patients with KCS2 and KCS1.[25,26] In contrast, some patients do not have hypoparathyroidism from early infancy, suggesting the presence of some parathyroid gland as in our patient I-1.[4,27] Furthermore, hypoparathyroidism may be secondary to hypomagnesemia as in our patient IV-13. Considering the fact that all of our 4 patients as well as another reported KCS2 case had hypomagnesemia,[4] FAM111A might be involved in magnesium homeostasis. Although further investigation is necessary to reveal the cause of hypoparathyroidism in KCS2, this study shows that a new gene, *FAM111A*, is indispensable for PTH development and/or regulation.

In conclusion, our finding that all 4 Japanese KCS2 patients we tested have the same de novo mutation (R569H) of *FAM111A* indicates that KCS2 is caused by a heterozygous mutation of *FAM111A*, and R569H is the hot spot mutation in patients with KCS2. Although the function of FAM111A is largely unknown, this study provides evidence that FAM111A is a key molecule for normal bone development, height gain, and PTH development and/or regulation. Our finding further creates a new research area in the fields associated with shared phenotypic features in KCS and different phenotypes between KCS1 and KCS2.

Disclosures

TI has received research grants and speaker's fees from Novo Nordisk and has received speaker's fees from Eli Lilly. SK has received research grants and speaker's fees from Novo Nordisk,

Pfizer, Eli Lilly, and JCR Pharmaceuticals and has received speaker's fees from Chugai Pharmaceutical. All other authors state that they have no conflicts of interest.

Acknowledgments

We thank the patients and their family members who participated in this study. We also thank Minako Takaki and Reiko Onai for technical support, and Mitsuko Itoh for kind assistance in English usage. This study was supported by a Grant-in-Aid from the Ministry of Education, Science, Sports, and Culture of Japan.

Authors' roles: Study design: TI and SK. Patients' sample and clinical data collection: YO, ET, AY, TY, and RH. Study conduct and data collection: TI, JM, and HI. Exome sequencing data analysis: JM, KD, JY, HI, SM, and ST. Data interpretation: TI, JM, KD, SM, ST, and SK. Study support and intellectual input: SM, ST, and SK. Drafting manuscript: TI. Revising manuscript content: SM, ST, and SK. Approving final version of manuscript: all authors. TI, SM, and SK take responsibility for the integrity of the data analysis.

References

1. Kenny FM, Linarelli L. Dwarfism and cortical thickening of tubular bones. Transient hypocalcemia in a mother and son. Am J Dis Child. 1966;111(2):201–7.
2. Caffey J. Congenital stenosis of medullary spaces in tubular bones and calvaria in two proportionate dwarfs—mother and son; coupled with transitory hypocalcemic tetany. Am J Roentgenol Radium Ther Nucl Med. 1967;100(1):1–11.
3. Fanconi S, Fischer JA, Wieland P, et al. Kenny syndrome: evidence for idiopathic hypoparathyroidism in two patients and for abnormal parathyroid hormone in one. J Pediatr. 1986;109(3):469–75.
4. Lee WK, Vargas A, Barnes J, Root AW. The Kenny-Caffey syndrome: growth retardation and hypocalcemia in a young boy. Am J Med Genet. 1983;14(4):773–82.
5. Franceschini P, Testa A, Bogetti G, et al. Kenny-Caffey syndrome in two sibs born to consanguineous parents: evidence for an autosomal recessive variant. Am J Med Genet. 1992;42(1):112–6.
6. Sabry MA, Zaki M, Abul Hassan SJ, et al. Kenny-Caffey syndrome is part of the CATCH 22 haploinsufficiency cluster. J Med Genet. 1998;35(1):31–6.
7. Sabry MA, Farag TI, Shaltout AA, et al. Kenny-Caffey syndrome: an Arab variant? Clin Genet. 1999;55(1):44–9.
8. Parvari R, Hershkovitz E, Grossman N, et al. Mutation of TBCE causes hypoparathyroidism-retardation-dysmorphism and autosomal recessive Kenny-Caffey syndrome. Nat Genet. 2002;32(3):448–52.
9. Tadaki H, Tokuhiro E, Shiga K, Kikuchi N, Mukai N, Fujieda K. A case of a 2-year-old girl with Kenny-Caffey Syndrome Type 2. Clin Pediatr Endocrinol. 2005;14(2 Suppl):22.
10. Oda Y, Ono R, Hiwatari M, Iwasaki H, Namai Y, Iimori Y. A case report: three-year-old boy of Kenny-Caffey Syndrome Type 2. Clin Pediatr Endocrinol. 2000;9(2):140.
11. Yorifuji T, Muroi J, Uematsu A. Kenny-Caffey syndrome without the CATCH 22 deletion. J Med Genet. 1998;35(12):1054.
12. Izumi Y, Tanae A, Kuratsuji T, et al. A case of 12-year-old boy with Kenny syndrome associated with hypomagnesemia and humoral immunodeficiency [in Japanese]. Shoninaika. 1987;19(10): 1503–2.
13. Unger S, Go´rna MW, Le Béchec A, et al. FAM111A mutations result in hypoparathyroidism and impaired skeletal development. Am J Hum Genet. 2013 May 14. [Epub ahead of print].
14. Li H, Durbin R. Fast and accurate short read alignment with Burrows-Wheeler transform. Bioinformatics. 2009;25(14):1754–60.
15. Li H, Handsaker B, Wysoker A, et al. The sequence alignment/map format and SAMtools. Bioinformatics. 2009;25(16):2078–9.
16. Kong A, Frigge ML, Masson G, et al. Rate of de novo mutations and the importance of father's age to disease risk. Nature. 2012;488(7412): 471–5.
17. Fine DA, Rozenblatt-Rosen O, Padi M, et al. Identification of FAM111A as an SV40 host range restriction and adenovirus helper factor. PLoS Pathog. 2012;8(10):e1002949.
18. Akamatsu S, Takata R, Haiman CA, et al. Common variants at 11q12, 10q26 and 3p11.2 are associated with prostate cancer susceptibility in Japanese. Nat Genet. 2012;44(4): 426–9, S421.
19. Shiang R, Thompson LM, Zhu YZ, et al. Mutations in the transmembrane domain of FGFR3 cause the most common genetic form of dwarfism, achondroplasia. Cell. 1994;78(2):335–42.
20. Weinstein LS, Shenker A, Gejman PV, Merino MJ, Friedman E, Spiegel AM. Activating mutations of the stimulatory G protein in the McCune-Albright syndrome. N Engl J Med. 1991;325(24):1688–95.
21. Gensure RC, Mäkitie O, Barclay C, Chan C, Depalma SR, Bastepe M, Abuzahra H, Couper R, Mundlos S, Sillence D, Ala Kokko L, Seidman JG, Cole WG, Jüppner H. A novel COL1A1 mutation in infantile cortical hyperostosis (Caffey disease) expands the spectrum of collagen-related disorders. J Clin Invest. 2005;115(5):1250–7.
22. Courtens W, Wuyts W, Poot M, Szuhai K, Wauters J, Reyniers E, Eleveld M, Diaz G, Nöthen MM, Parvari R. Hypoparathyroidism-retardation-dysmorphism syndrome in a girl: A new variant not caused by a TBCE mutation--clinical report and review. Am J Med Genet A. 2006; 140(6):611–7.
23. Shoback D, Clinical practice. Hypoparathyroidism. N Engl J Med. 2008;359(4):391–403.
24. Zajac JD, Danks JA. The development of the parathyroid gland: from fish to human. Curr Opin Nephrol Hypertens. 2008;17(4):353–6.
25. Boynton JR, Pheasant TR, Johnson BL, Levin DB, Streeten BW. Ocular findings in Kenny's syndrome. Arch Ophthalmol. 1979;97(5): 896–00.
26. Parvari R, Diaz GA, Hershkovitz E. Parathyroid development and the role of tubulin chaperone E. Horm Res. 2007;67(1):12–21.
27. Wilson MG, Maronde RF, Mikity VG, Shinno NW. Dwarfism and congenital medullary stenosis (Kenny syndrome). Birth Defects Orig Artic Ser. 1974;10(12):128–32.

Efficacy of the anti–IL-6 receptor antibody tocilizumab in neuromyelitis optica

A pilot study

OPEN

Manabu Araki, MD, PhD
Takako Matsuoka, MD
Katsuichi Miyamoto, MD, PhD
Susumu Kusunoki, MD, PhD
Tomoko Okamoto, MD, PhD
Miho Murata, MD, PhD
Sachiko Miyake, MD, PhD
Toshimasa Aranami, MD, PhD
Takashi Yamamura, MD, PhD

Correspondence to Dr. Yamamura: yamamura@ncnp.go.jp

ABSTRACT

Objective: To evaluate the safety and efficacy of a humanized anti-interleukin-6 receptor antibody, tocilizumab (TCZ), in patients with neuromyelitis optica (NMO).

Methods: Seven patients with anti-aquaporin-4 antibody (AQP4-Ab)-positive NMO or NMO spectrum disorders were recruited on the basis of their limited responsiveness to their current treatment. They were given a monthly injection of TCZ (8 mg/kg) with their current therapy for a year. We evaluated the annualized relapse rate, the Expanded Disability Status Scale score, and numerical rating scales for neurogenic pain and fatigue. Serum levels of anti-AQP4-Ab were measured with AQP4-transfected cells.

Results: Six females and one male with NMO were enrolled. After a year of TCZ treatment, the annualized relapse rate decreased from 2.9 ± 1.1 to 0.4 ± 0.8 ($p < 0.005$). The Expanded Disability Status Scale score, neuropathic pain, and general fatigue also declined significantly. The ameliorating effects on intractable pain exceeded expectations.

Conclusion: Interleukin-6 receptor blockade is a promising therapeutic option for NMO.

Classification of evidence: This study provides Class IV evidence that in patients with NMO, TCZ reduces relapse rate, neuropathic pain, and fatigue. *Neurology*® 2014;82:1302–1306

GLOSSARY

Ab = antibody; **AQP4** = aquaporin-4; **AZA** = azathioprine; **EDSS** = Expanded Disability Status Scale; **IL** = interleukin; **IL-6R** = interleukin-6 receptor; **NMO** = neuromyelitis optica; **PB** = plasmablasts; **PSL** = prednisolone; **TCZ** = tocilizumab.

Neuromyelitis optica (NMO) is a relatively rare autoimmune disease that predominantly affects the spinal cord and optic nerve. Anti–aquaporin-4 antibody (AQP4-Ab), which is a disease marker of NMO, has an important role in causing the destruction of astrocytes that express AQP4.[1] Empirically, the use of disease-modifying drugs for multiple sclerosis, including interferon β, is not recommended for NMO,[2] which is consistent with the distinct pathogenesis of NMO and multiple sclerosis. We have recently described that plasmablasts (PB), which are a subpopulation of B cells, increased in the peripheral blood of patients with NMO and that PB are a major source of anti-AQP4-Ab among peripheral blood B cells.[3] In addition, we observed that exogenous interleukin (IL)-6 promotes the survival of PB and their production of anti-AQP4-Ab in vitro. Given the increased levels of IL-6 in the serum and CSF during relapses of NMO,[1,3] we postulated that blocking IL-6 receptor (IL-6R) pathways might reduce the disease activity of NMO by inactivating the effector functions of PB. A humanized anti–IL-6R monoclonal antibody, tocilizumab (TCZ) (Actemra/RoActemra), has been approved in more than 100 countries for use in the treatment of rheumatoid arthritis.[4] Herein, we describe our clinical study that aimed to explore the efficacy of TCZ in NMO.

Editorial, page 1294

From the Multiple Sclerosis Center (M.A., T.O., S.M., T.A., T.Y.) and Department of Neurology (T.O., M.M.), National Center Hospital, and Department of Immunology, National Institute of Neuroscience (T.M., S.M., T.A., T.Y.), National Center of Neurology and Psychiatry, Tokyo; Department of Neurology (K.M., S.K.), Kinki University School of Medicine, Osaka; and Department of Pediatrics (T.M.), Graduate School of Medicine, University of Tokyo, Japan.

Go to Neurology.org for full disclosures. Funding information and disclosures deemed relevant by the authors, if any, are provided at the end of the article.

This is an open access article distributed under the terms of the Creative Commons Attribution-Noncommercial No Derivative 3.0 License, which permits downloading and sharing the work provided it is properly cited. The work cannot be changed in any way or used commercially.

© 2014 American Academy of Neurology

© 2014 American Academy of Neurology. Unauthorized reproduction of this article is prohibited.

Table Demographics of the patients

	Patient						
	1	2	3	4	5	6	7
Age, y/sex	37/F	38/F	26/F	31/M	55/F	62/F	23/F
Age at onset, y	23	27	21	12	38	60	21
Anti-AQP4-Ab	+	+	+	+	+	+	+
Myelitis	+	+	+	+	+	+	–
Optic neuritis	+	+	+	+	+	+	+
EDSS score	3.5	6.5	3.5	6.0	6.5	6.5	3.0
Total no. of relapses	20	9	6	16	20	3	7
ARR before TCZ	3	2	2	2	3	3	5
Immunotherapies for exacerbations	IVMP, PLEX	IVMP, PLEX	IVMP, PLEX	IVMP, OBP, PLEX	IVMP, PLEX	IVMP, PLEX	IVMP, PLEX
Past immunotherapies	IFNβ, IVIg	IFNβ	—	IFNβ, MITX	IFNβ, AZA	—	AZA
Present immunotherapies	PSL, AZA	AZA	PSL	PSL, AZA	PSL, CyA	PSL, CyA	PSL, tacrolimus
Neuropathic pain (e.g., girdle pain), NRS	4	4	2	4	4	3	0
General fatigue, NRS	5	8	6	7	5	3	9
Pain and antispasticity medication	GBP, CZP, NTP, NSAID	CZP, mexiletine, NTP, tizanidine, NSAID	—	CBZ, baclofen, NSAID	CBZ	PGB	—

Abbreviations: AQP4-Ab = aquaporin-4 antibody; ARR = annualized relapse rate; AZA = azathioprine; CBZ = carbamazepine; CZP = clonazepam; CyA = cyclosporine; EDSS = Expanded Disability Status Scale; GBP = gabapentin; IFNβ = interferon β; IVIg = IV immunoglobulin; IVMP = IV methylprednisolone; MITX = mitoxantrone; NRS = numerical rating scale; NSAID = nonsteroidal anti-inflammatory drug; NTP = Neurotropin (an extract from the inflamed skin of vaccinia virus–inoculated rabbits); OBP = oral betamethasone pulse therapy; PGB = pregabalin; PLEX = plasma exchange; PSL = prednisolone; TCZ = tocilizumab.

METHODS

Level of evidence. The aim of this Class IV evidence study was to evaluate the effect and safety of a monthly injection of TCZ (8 mg/kg) with their current therapy in patients with NMO. We evaluated the adverse events based on Common Terminology Criteria for Adverse Events, version 4.0.

Standard protocol approvals, registrations, and patient consents. All patients gave written informed consent before the first treatment with TCZ. The institutional ethical standards committee on human experimentation approved this clinical study. The study is registered with University Hospital Medical Information Network Clinical Trials Registry, numbers UMIN000005889 and UMIN000007866.

Patients and treatment. Seven patients who met the diagnostic criteria of NMO in 2006 were enrolled after providing informed consent (table). Results of chest x-rays, interferon γ release assays, and plasma 1,3-β-D-glucan measurement excluded latent tuberculosis and fungal infection. All of the patients had been treated with combinations of oral prednisolone (PSL) and immunosuppressants, including azathioprine (AZA). Nevertheless, they had at least 2 relapses during the year before enrollment (figure 1). Among their past immunomodulatory medications, interferon β had been prescribed in 4 patients before the anti-AQP4-Ab assay became available. Although symptomatic treatments had been provided, the patients experienced general fatigue and intractable pain in their trunk and limbs. There were no abnormalities in their routine laboratory blood tests. Neither pleocytosis nor increased levels of IL-6 were observed in the CSF. MRI revealed high-intensity signals in the optic nerves and longitudinally extensive lesions in the spinal cord. All patients except one had scattered brain lesions. A monthly dose (8 mg/kg) of TCZ was added to the patients' oral corticosteroid and immunosuppressive drug regimen.

Clinical and laboratory assessment. As clinical outcome measures, we evaluated alterations in the number of relapses, Expanded Disability Status Scale (EDSS) scores, and pain and fatigue severity scores (numerical rating scales). A relapse was defined as an objective exacerbation in neurologic findings that lasted for longer than 24 hours with an increase in the EDSS score of more than 0.5. Brain and spinal cord MRI scans were examined every 4 or 6 months. CSF examinations, sensory-evoked potentials, and visual-evoked potentials were also evaluated at the time of entry into the study and 12 months later. We measured serum anti-AQP4-Ab levels by evaluating the binding of serum immunoglobulin G to AQP4 transfectants, as previously described.[5] All outcome measures were analyzed with nonparametric Wilcoxon rank-sum tests, with the use of 2-tailed statistical tests at a significance level of 0.05.

RESULTS

After starting TCZ treatment, the total number of annual relapses in the patients significantly reduced (figures 1 and 2). Notably, 5 of the 7 patients were relapse-free after starting TCZ. The relapses observed in patients 1 and 5 were mild and their symptoms recovered after IV methylprednisolone. On average, the annualized relapse rate reduced from 2.9 ± 1.1 (range, 2–5) during the year before study to 0.4 ± 0.8 (range, 0–2) during the year after

© 2014 American Academy of Neurology. Unauthorized reproduction of this article is prohibited.

Figure 1 Clinical course of the patients before and after tocilizumab treatment

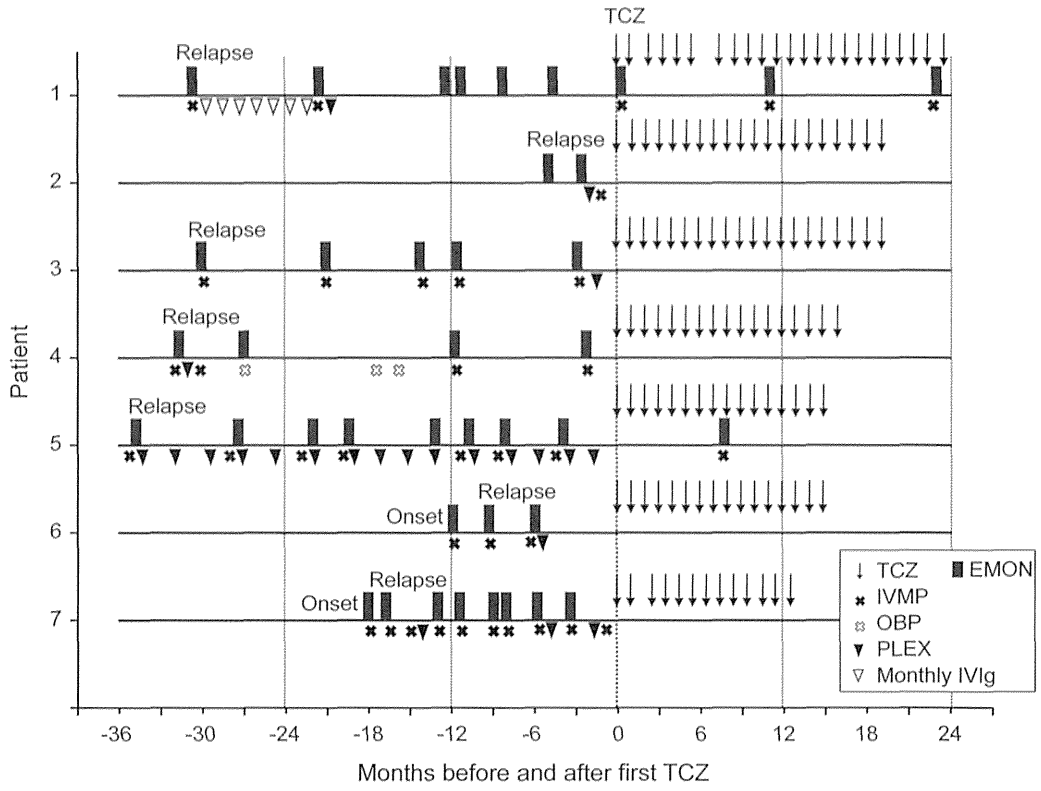

The zero on the x-axis represents the first administration of tocilizumab (TCZ). Dark gray bars: exacerbations of myelitis or optic neuritis (EMON); downward arrow: TCZ treatment; black X: IV methylprednisolone (IVMP); white X: oral betamethasone pulse (OBP) therapy; black triangle: plasma exchange (PLEX); white triangle: IV immunoglobulin (IVIg). After receiving 12 injections, all patients continued treatment with TCZ by entering an extension study that evaluates the long-term safety and efficacy of TCZ. We showed the clinical status after completion of the 1-year study to indicate the continuation of remission.

starting TCZ (figure 2). The EDSS score decreased modestly but significantly from 5.1 ± 1.7 (range, 3.0–6.5) to 4.1 ± 1.6 (range, 2.0–6.0) at 12 months. The chronic neurogenic pain in their trunk and extremities, which is characteristic of NMO[6,7] (table), gradually lessened after the patients started TCZ. Consequently, the numerical rating scale for pain reduced from 3.0 ± 1.5 upon study entry to 1.3 ± 1.3 after 6 months and 0.9 ± 1.2 after 12 months. General fatigue also improved from 6.1 ± 2.0 to 3.9 ± 2.1 at 6 months and 3.0 ± 1.4 at 12 months. The MRI scans, sensory- and visual-evoked potentials, and CSF observations did not show any interval changes. Serum anti-AQP4-Ab levels represented by the relative mean fluorescence intensity were significantly reduced (figure 2E).

Adverse events included upper respiratory infections (patients 1 and 7), acute enterocolitis (patients 1 and 4), acute pyelonephritis (patient 1), leukocytopenia and/or lymphocytopenia (patients 1, 4, and 7), anemia (patients 3 and 7), and a slight decline in systolic blood pressure (patient 1). However, none of the events was severe. Oral PSL and AZA were tapered in patients 1, 3, 4, and 7, resulting in a reduction of the mean doses (PSL from 19.5 ± 7.6 to 8.8 ± 5.6 mg/d [average of patients 1, 3, 4, and 7], AZA from 37.5 to 5.4 mg/d [average of patients 1 and 4]).

DISCUSSION Pain management is a difficult problem in patients with NMO. In fact, a retrospective study of 29 patients with NMO who experienced pain has documented that 22 of the 29 patients were taking pain medications, but none of them rated their current pain as 0 out of 10 on a 10-point scale.[6] In the present study, the intractable pain reduced gradually after the patients started TCZ treatment. After 6 or 12 months of therapy, 3 of the 6 patients with pain were completely free of pain. These results suggested a role of IL-6 in NMO pain and the possible merits of the use of TCZ in clinical practice as a pain reliever.

The pathophysiology of neurogenic pain is now understood in the context of interactions between the immune and nervous systems,[8] which involve proinflammatory cytokines such as IL-6 as well as immune cells, activated glia cells, and neurons. Supportive for the role of IL-6 in pain, recent work in

© 2014 American Academy of Neurology. Unauthorized reproduction of this article is prohibited.

Figure 2 **Effects of tocilizumab on clinical and immunologic parameters**

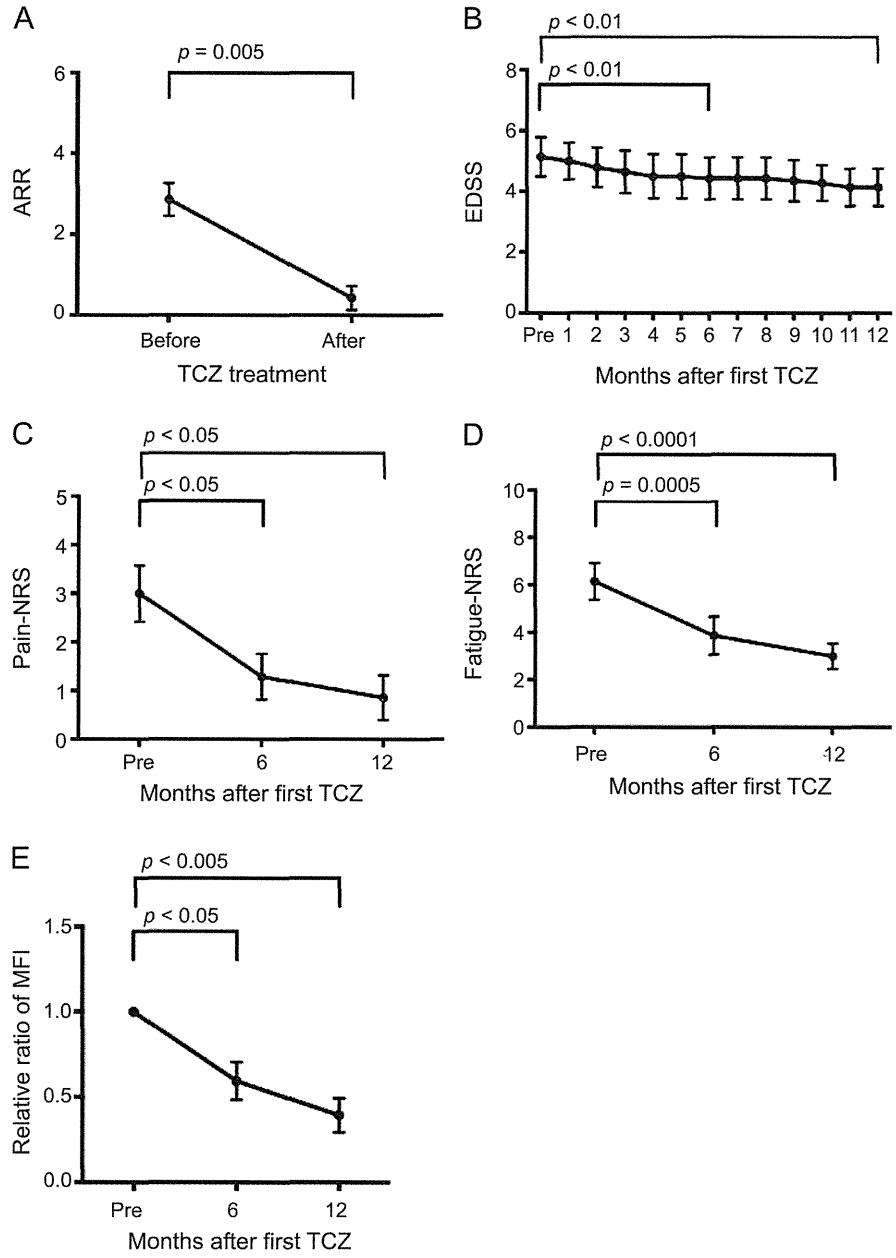

(A) Annualized relapse rate (ARR) before and after tocilizumab (TCZ) treatment. (B) Expanded Disability Status Scale (EDSS) score during the 1-year study period. Pain severity (numerical rating scale [NRS]) (C) and fatigue severity (D) scores before, 6 months after, and 12 months after the start of TCZ treatment. The dots and I bars indicate means ± SEM. We analyzed only data obtained during the first year of TCZ treatment. (E) The alterations in the serum anti-aquaporin-4 antibody (AQP4-Ab) were evaluated by the relative ratio of the mean fluorescence intensity (MFI), which was based on the MFI before TCZ treatment. Serum anti-AQP4-Ab detection assay was performed as described previously[3,5] with minor modifications. In brief, optimally diluted serum was added to human AQP4-expressing Chinese hamster ovary (CHO) cells. CHO cell-bound anti-AQP4-Ab was detected using fluorescein isothiocyanate–anti-human immunoglobulin G antibody by flow cytometry. For comparison, the MFI of each sample was divided by the MFI of the sample before the start of TCZ treatment.

rodents showed that gp130 expressed by nociceptive neurons might have a key role in pathologic pain.[9] Although expression of membrane-bound IL-6R is restricted to hepatocytes, neutrophils, and subsets of T cells, the gp130, ubiquitously expressed in cellular membranes, can transduce IL-6R signaling via binding to the IL-6/soluble IL-6R complex.[4] This indicates that IL-6 trans-signaling via the soluble IL-6R could be pivotal in causing pain in NMO, although alternative possibilities cannot be excluded.

TCZ treatment recently showed efficacy for patients with aggressive NMO who were refractory to the anti-CD20 antibody rituximab.[10] The efficacy of TCZ could result from its effect on IL-6–dependent inflammatory

© 2014 American Academy of Neurology. Unauthorized reproduction of this article is prohibited.

processes, involving CD20-negative PB, pathogenic T cells, and regulatory T cells. This work, however, does not restrict the use of TCZ in serious NMO. Although the need for monitoring latent infection and adverse events is obvious, we propose that the use of TCZ may be considered at an early stage of NMO before disability or a lower quality of life becomes evident.

AUTHOR CONTRIBUTIONS

T.Y., S.M., S.K., M.M., and M.A.: design and conceptualization of the study. M.A., K.M., T.O., and T.Y.: analysis and internalization of the data. T.M. and T.A.: flow cytometry analysis and anti-AQP4-Ab assay. M.A. and T.Y.: drafting and revising of the manuscript. T.Y.: supervising the entire project.

STUDY FUNDING

Supported by the Health and Labour Sciences Research Grants on Intractable Diseases (Neuroimmunological Diseases) and on Promotion of Drug Development from the Ministry of Health, Labour and Welfare of Japan.

DISCLOSURE

M. Araki has received honoraria from Novartis. T. Matsuoka reports no disclosures relevant to the manuscript. K. Miyamoto has received honoraria from Novartis, Bayer, and Biogen Idec. S. Kusunoki serves as an editorial board member of *Experimental Neurology*, *Journal of Neuroimmunology*, and *Neurology & Clinical Neuroscience* (associate editor). He received honoraria from Teijin Pharma, Nihon Pharmaceuticals, Japan Blood Products Organization, Novartis Pharma, Dainippon Sumitomo Pharma, Kyowa Kirin, Asahi Kasei, Bayer, Sanofi, and GlaxoSmithKline. He is funded by research grants from the Ministry of Health, Labour and Welfare, Japan, and grants from the Japan Science and Technology Agency and the Ministry of Education, Culture, Sports, Science and Technology, Japan. He received research support from Novartis, GlaxoSmithKline, Dainippon Sumitomo Pharma, Teijin Pharma, Astellas, Sanofi, Japan Blood Products Organization, and Nihon Pharmaceuticals. T. Okamoto reports no disclosures relevant to the manuscript. M. Murata received honoraria for consulting and/or lecturing from GlaxoSmithKline Co., Ltd., Boehringer Ingelheim Co., Ltd., Dainippon Sumitomo Pharma Co., Ltd., Novartis Pharma, and Hisamitsu Pharma. S. Miyake has received speaker honoraria from Biogen Idec, Pfizer Inc., and Novartis Pharma. T. Aranami reports no disclosures relevant to the manuscript. T. Yamamura has served on scientific advisory boards for Biogen Idec and Chugai Pharmaceutical Co., Ltd.; has received research support from Ono Pharmaceutical Co., Ltd., Chugai Pharmaceutical Co., Ltd., Teva Pharmaceutical K.K., Mitsubishi Tanabe Pharma Corporation, and Asahi Kasei Kuraray Medical Co., Ltd.; has received speaker honoraria from Novartis Pharma, Nihon Pharmaceutical Co., Ltd., Santen Pharmaceutical Co., Ltd., Abbott Japan Co., Ltd./Eisai Co., Ltd., Biogen Idec, Dainippon Sumitomo Pharma Co., Ltd., Mitsubishi Tanabe Pharma Corporation, Bayer Holding Ltd., and Astellas Pharma Inc. Go to Neurology.org for full disclosures.

Received September 4, 2013. Accepted in final form December 2, 2013.

REFERENCES

1. Jarius S, Wildemann B. AQP4 antibodies in neuromyelitis optica: diagnostic and pathogenetic relevance. Nat Rev Neurol 2010;6:383–392.
2. Okamoto T, Ogawa M, Lin Y, et al. Treatment of neuromyelitis optica: current debate. Ther Adv Neurol Disord 2008;1:5–12.
3. Chihara N, Aranami T, Sato W, et al. Interleukin 6 signaling promotes anti-aquaporin 4 autoantibody production from plasmablasts in neuromyelitis optica. Proc Natl Acad Sci U S A 2011;108:3701–3706.
4. Tanaka T, Narazaki M, Kishimoto T. Therapeutic targeting of the interleukin-6 receptor. Annu Rev Pharmacol Toxicol 2012;52:199–219.
5. Araki M, Aranami T, Matsuoka T, et al. Clinical improvement in a patient with neuromyelitis optica following therapy with the anti-IL-6 receptor monoclonal antibody tocilizumab. Mod Rheumatol 2013;23:827–831.
6. Qian P, Lancia S, Alvarez E, et al. Association of neuromyelitis optica with severe and intractable pain. Arch Neurol 2012;69:1482–1487.
7. Kanamori Y, Nakashima I, Takai Y, et al. Pain in neuromyelitis optica and its effect on quality of life: a cross-sectional study. Neurology 2011;77:652–658.
8. Vallejo R, Tilley DM, Vogel L, et al. The role of glia and immune system in the development and maintenance of neuropathic pain. Pain Pract 2010;10:167–184.
9. Andratsch M, Mair N, Constantin CE, et al. A key role for gp130 expressed on peripheral sensory nerves in pathological pain. J Neurosci 2009;29:13473–13483.
10. Ayzenberg I, Kleiter I, Schröder A, et al. Interleukin 6 receptor blockade in patients with neuromyelitis optica nonresponsive to anti-CD20 therapy. JAMA Neurol 2013;70:394–397.

The Premier Event for *the* Latest Research on Concussion

Registration is now open for The Sports Concussion Conference—*the* premier event on sports concussion from the American Academy of Neurology—set for July 11 through 13, 2014, at the Sheraton Chicago Hotel & Towers in Chicago. You won't want to miss this one-of-a-kind opportunity to learn the very latest scientific advances in diagnosing and treating sports concussion, post-concussion syndrome, chronic neurocognitive impairment, and controversies around gender issues and second impact syndrome from the world's leading experts on sports concussion. Early registration ends June 9, 2014. Register today at *AAN.com/view/ConcussionConference*.

© 2014 American Academy of Neurology. Unauthorized reproduction of this article is prohibited.

Article

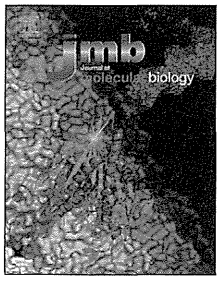

Structural Basis for the Specific Recognition of the Major Antigenic Peptide from the Japanese Cedar Pollen Allergen Cry j 1 by HLA-DP5

Seisuke Kusano[1,2], Mutsuko Kukimoto-Niino[1,2], Yoko Satta[3], Noboru Ohsawa[1,2], Tomomi Uchikubo-Kamo[1,2], Motoaki Wakiyama[1,2], Mariko Ikeda[1,2], Takaho Terada[1,4], Ken Yamamoto[5], Yasuharu Nishimura[6], Mikako Shirouzu[1,2], Takehiko Sasazuki[7] and Shigeyuki Yokoyama[1,4]

*1 - **RIKEN Systems and Structural Biology Center,** 1-7-22 Suehiro-cho, Tsurumi-ku, Yokohama 230-0045, Japan*
*2 - **Division of Structural and Synthetic Biology,** RIKEN Center for Life Science Technologies, 1-7-22 Suehiro-cho, Tsurumi-ku, Yokohama 230-0045, Japan*
*3 - **Department of Evolutionary Studies of Biosystems,** Center for Promotion of Integrated Sciences, The Graduate University for Advanced Studies, Shonan Village, Hayama, Kanagawa 240-0193, Japan*
*4 - **RIKEN Structural Biology Laboratory,** 1-7-22 Suehiro-cho, Tsurumi-ku, Yokohama 230-0045, Japan*
*5 - **Division of Genome Analysis,** Research Center for Genetic Information, Medical Institute of Bioregulation, Kyushu University, 3-1-1 Maidashi, Higashi-ku, Fukuoka 812-8582, Japan*
*6 - **Department of Immunogenetics,** Graduate School of Medical Sciences, Kumamoto University, 1-1-1 Honjo, Chuo-ku, Kumamoto 860-8556, Japan*
*7 - **Institute for Advanced Study,** Kyushu University, 3-1-1 Maidashi, Higashi-ku, Fukuoka 812-8582, Japan*

***Correspondence to Shigeyuki Yokoyama:** RIKEN Structural Biology Laboratory, 1-7-22 Suehiro-cho, Tsurumi-ku, Yokohama 230-0045, Japan. yokoyama@riken.jp*
http://dx.doi.org/10.1016/j.jmb.2014.06.020
Edited by S. Koide

Abstract

The major allergen, Cry j 1, was isolated from Japanese cedar *Cryptomeria japonica* (Cry j) pollen and was shown to react with immunoglobulin E antibodies in the sera from pollinosis patients. We previously reported that the frequency of HLA-DP5 was significantly higher in pollinosis patients and the immunodominant peptides from Cry j 1 bound to HLA-DP5 to activate Th2 cells. In the present study, we determined the crystal structure of the HLA-DP5 heterodimer in complex with a Cry j 1-derived nine-residue peptide, at 2.4 Å resolution. The peptide-binding groove recognizes the minimal peptide with 10 hydrogen bonds, including those between the negatively charged P1 pocket and the Lys side chain at the first position in the peptide sequence. We confirmed that HLA-DP5 exhibits the same Cry j 1-binding mode in solution, through pull-down experiments using structure-based mutations of Cry j 1. We also identified the characteristic residues of HLA-DP5 that are responsible for the distinct properties of the groove, by comparing the structure of HLA-DP5 and the previously reported structures of HLA-DP2 in complexes with pDRA of the self-antigen. The comparison revealed that the HLA-DP5·pCry j 1 complex forms several hydrogen bond/salt bridge networks between the receptor and the antigen that were not observed in the HLA-DP2·pDRA complex. Evolutionary considerations have led us to conclude that HLA-DP5 and HLA-DP2 represent two major groups of the HLA-DP family, in which the properties of the P1 and P4 pockets have evolved and acquired the present ranges of epitope peptide-binding specificities.

© 2014 The Authors. Published by Elsevier Ltd. This is an open access article under the CC BY-NC-ND license (http://creativecommons.org/licenses/by-nc-nd/3.0/).

Introduction

Plant pollens are the most common causes of prevalent type I hypersensitivity (allergy) diseases, which induce seasonal rhinitis and conjunctivitis in humans [1–3]. *Dactylis gromerata* and *Ambrosia artemisiifolia* (ragweed) pollens cause the two major hay fevers endured internationally, while

0022-2836/© 2014 The Authors. Published by Elsevier Ltd. This is an open access article under the CC BY-NC-ND license (http://creativecommons.org/licenses/by-nc-nd/3.0/).

Cryptomeria japonica (Cry j, Japanese cedar) pollen is the most prevalent allergen in Japan [4], with respect to the number of pollinosis patients. In particular, the number of Japanese cedar pollinosis patients has rapidly increased since the 1960s in Japan [5], and presently, more than 25 million people suffer through the months from February to April, when the pollen is dispersed [6]. So far, three major allergens, Cry j 1 [7], Cry j 2 [8], and Cry j 3 [9], have been isolated from the cedar pollen and have been shown to react with immunoglobulin E (IgE) antibodies from the pollinosis patients [9,10]. Cry j 1 and Cry j 2 are 37–45 kDa basic glycoproteins [11], and they share 70–80% amino acid sequence identity with each other [11]. They were identified as a pectate lyase (isozyme) [12] and a polymethylgalacturonase (enzyme) [13], respectively.

IgE is responsible for inducing type I hypersensitivity (allergic) diseases [14]. Secretion of antibodies, including IgE, by plasma cells requires interactions between antigen-activated B cells and antigen-activated $CD4^+$ type 2 helper T (Th2) cells, to allow the differentiation of plasma cells from B cells. $CD4^+$ T cells are activated by the recognition of immunogenic peptides presented by class II human leukocyte antigen (HLA) molecules on the surface of antigen-presenting cells [15]. The allergen-specific IgE production completely depends on the class switch of the immunoglobulin gene in plasma cells, and this is mediated by a cytokine, interleukin-4, produced by $CD4^+$ Th2 cells upon the recognition of allergen-derived peptides in the context of class II HLA molecules.

The class II HLA molecules are heterodimers of the α and β chains and are encoded by genes in the class II HLA region on the short arm of chromosome 6 [16]. The class II HLA molecules are classified into three isotypes, HLA-DR, HLA-DQ, and HLA-DP. In HLA-DR, the polymorphic variation is primarily provided by the β chain, rather than the α chain [17]. On the other hand, in HLA-DQ and HLA-DP, both the α and β chains are polymorphic, and thus, a variety of HLA-DQA/DQB and HLA-DPA/DPB haplotypes are formed [17]. The crystal structures of class II HLA complexes with non-self-peptides derived from a plant have been determined for the HLA-DQ2•deamidated-gliadin [18], the HLA-DQ2.3•Gamma-gliadin [19], and the HLA-DQ8•deamidated-glutein [20,21]. Nine specific amino acid residues in each peptide are accommodated in the peptide-binding groove, formed by the α and β chains.

We previously analyzed the statistical association between Japanese cedar pollinosis and class II HLA alleles and found that the patients possess the HLA-DP5 (*DPA1*02:02* and *DPB1*05:01*) at a rate of about 80% [22]. Furthermore, we also identified an immunodominant peptide that induces HLA-DP5-restricted Th2 cells, among 38 synthesized overlapping 13-residue peptides spanning the entire length of Cry j 1. The minimal peptide sequence for the HLA-DP5-restricted Th cells was suggested to be nine residues, 214-KVTVAFNQF-222, of Cry j 1 [22]. Therefore, we thought that the HLA-DP5-associated susceptibility to Japanese cedar pollinosis may be explained by the following phenomenon: HLA-DP5-mediated antigen presentation of the major Cry j 1 epitope to Th2 cells producing interleukin-4, an essential cytokine for IgE production by antibody-secreting plasma cells. Subsequently, it was reported that a large number of Cry j 1 and Cry j 2 peptides were associated with various class II HLA allelic products. Among the HLA-DP family members, only HLA-DP5 and HLA-DP2 were shown to be associated with the Cry j antigenic peptides [23,24]. However, the structural mechanisms of specific peptide recognition are still unknown, for not only the peptides of the Cry j antigens but also those of other pollen antigens. The only peptide-bound HLA-DP structure available is that of HLA-DP2 (*DPA1*01:03* and *DPB1*02:01*) in complex with pDRA derived from the self-HLA-DR α chain [25].

In the present study, we determined the crystal structure of the extracellular region of the HLA-DP5 (*DPA1*02:02* and *DPB1*05:01*) heterodimer, in complex with the Cry j 1-derived nine-residue peptide, KVTVAFNQF, at 2.4 Å resolution. The peptide-binding groove specifically formed by the HLA-DP5α and HLA-DP5β chains captures the minimal peptide KVTVAFNQF with 10 hydrogen bonds, including those between the negatively charged P1 pocket and the Lys side chain at the first anchoring position in the peptide sequence. This binding mode was confirmed *in vitro*, by mutations of the Cry j 1 residues facing the peptide-binding groove of HLA-DP5 in the crystal structure. Furthermore, we identified the characteristic residues of HLA-DP5 that are responsible for the distinct properties of the groove, by comparing the structure of HLA-DP5 and the previously reported structure of HLA-DP2 (*DPA1*01:03* and *DPB1*02:01*) in complex with pDRA. The comparison revealed that the HLA-DP5•Cry j 1 complex forms several hydrogen bond/salt bridge networks between the receptor and the antigen that were not observed in the HLA-DP2•pDRA complex. Thus, the specific HLA-DP–antigenic peptide binding mechanism has been established.

Results

Overall structure of the complex of HLA-DP5 with the Cry j 1 peptide

We prepared a plasmid encoding the HLA-DP5 α chain extracellular region (residues 1–181) and the HLA-DP5 β chain extracellular region (residues 4–189) with the N-terminus fused to a nine-amino-acid residue

Table 1. Crystallographic data collection and refinement statistics

	HLA-DP5•Cry j 1(9-mer)
Data collection	
Space group	*P*1
Cell dimensions	
a, *b*, *c* (Å)	61.2, 64.4, 130.4
α, β, γ (°)	93.0, 97.5, 109.4
Resolution (Å)	64–2.4 (2.49–2.40)[a,b]
R_{sym}	0.116 (0.563)
$I/\sigma I$	12.3 (3.05)
Completeness (%)	97.4 (95.6)
Redundancy	3.5 (3.4)
Refinement	
Resolution (Å)	64.0–2.4
No. of reflections	70,445
R_{work}/R_{free}	0.201/0.237
No. of atoms	
Protein	12,380
Ligand	56
Water	267
B-factors	
Protein	29.1
Ligand	27.6
Water	29.8
rmsd	
Bond lengths (Å)	0.005
Bond angles (°)	1.07

[a] One crystal was used for data collection and refinement.
[b] Values in parentheses are for the highest-resolution shell.

Cry j 1 peptide (KVTVAFNQF) and co-expressed the two chains by the baculovirus–insect cell expression system. It was assumed that the α and β chains of HLA-DP5 form a "heterodimer" and that the peptide fused to the β chain is accommodated in the binding site formed by the two chains. The HLA-DP5•Cry j 1(9-mer) complex was purified and crystallized as described in Materials and Methods, and the structure was determined at 2.4 Å resolution. The statistics for the data collection and the refined model is shown in Table 1. The asymmetric unit of the HLA-DP5•Cry j 1(9-mer) crystal contains four complexes, *A*, *B*, *C*, and *D*. Each complex superposed on another with a root-mean-square deviation (rmsd) value of ~0.8 Å for the C_α atoms. Therefore, the structure of complex *A* is described hereafter. The α and β chains consist of the α1 and α2 domains and the β1 and β2 domains, respectively (Fig. 1a). The α1 and β1 domains form the peptide-binding cleft, and the α2 and β2 domains form the heterodimeric interface (Fig. 1a and b). An *N*-acetyl-D-glucosamine moiety is attached to Asn118 (α2 domain) in HLA-DP5•Cry j 1(9-mer) (Fig. 1a). The overall structures of the HLA-DP5 heterodimers are similar to those of the class II HLA heterodimers [26], including HLA-DP2.

In the HLA-DP5•Cry j 1(9-mer) structure, the nine residues of the accommodated Cry j 1 peptide (KVTVAFNQF) are clearly visible in the electron density map and occupy the p1-to-p9 binding pockets (Fig. 1b and c). Lys(p1), Phe(p6), and Phe(p9) are the "anchoring residues", and their side chains are buried within their corresponding pockets formed along the peptide-binding groove of HLA-DP5 (Fig. 1c). In solution, the purified HLA-DP5•Cry j 1(9-mer) complex exists as a single

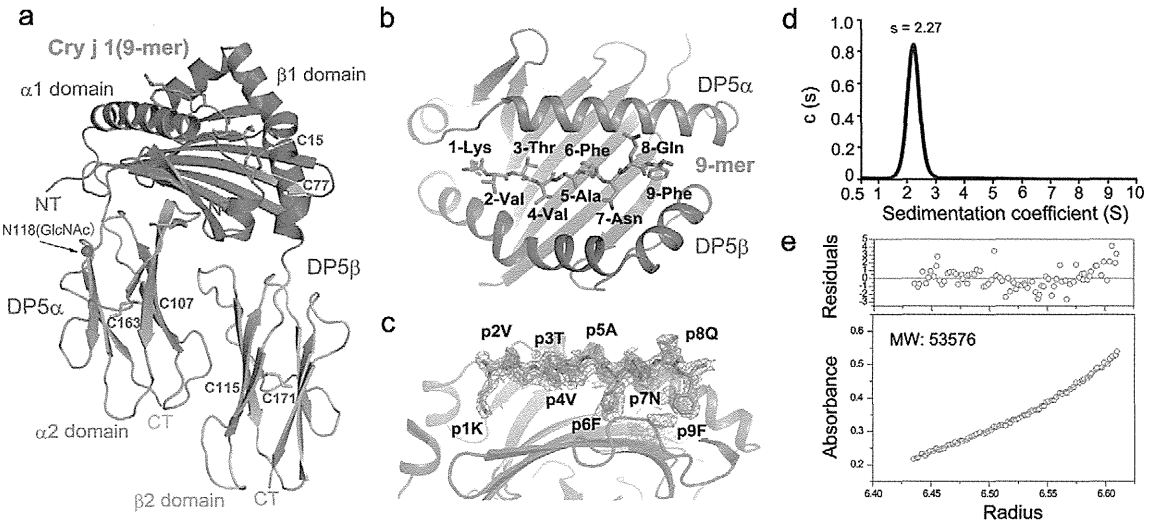

Fig. 1. Crystal structure of the HLA-DP5•Cry j 1 complex. (a–c) The HLA-DP5•Cry j 1(214–222) complex structure. Extracellular domains of the HLA-DP5α and HLA-DP5β chains are shown as ribbon models in green (α1) and light green (α2) and in blue (β1) and light blue (β2), respectively. The Cry j 1(9-mer) peptide is represented by orange sticks. (a) Overall structure. (b) Top views of the peptides in the peptide-binding groove. (c) Side views of the peptides in the peptide-binding groove. The $2F_o - F_c$ electron density maps, contoured at 1.5σ, are shown as a cyan mesh (before refinement) and an olive mesh (after refinement) within 1.0 Å of the peptide. (d and e) Analytical ultracentrifugation of the HLA-DP5•Cry j 1(9-mer) complex. (d) Distribution of sedimentation coefficients (*s*) by sedimentation velocity experiments. (e) A plot of the sedimentation equilibrium data with the residuals from the best fit to a single ideal species.

complex species, as revealed by analytical ultracentrifugation (Fig. 1d and e).

Binding mode of HLA-DP5•Cry j 1(9-mer)

The Cry j 1 peptide interacts extensively with the side chains from the HLA-DP5 groove, involving a total of 10 hydrogen bonds, with four formed by the p1, p7, and p8 side chains and six mediated by the p2, p4, p5, and p7 main chains of the peptide (Fig. 2a). Actually, in common mostly with the peptide•HLA-DR1 complexes, five hydrogen bonds are observed between the main chain of the Cry j 1 peptide and the side chains of HLA-DP5: p2 and Tyr9(α), p2 and Asn80(β), p4 and Asn62(α), p5 and Lys69(β), and p7 and Asn69(α). Moreover, the other five hydrogen bonds are formed between the side chains of the peptide and HLA-DP5. This binding by an extensive hydrogen bonding network is in sharp contrast to the binding of the pDRA peptide with HLA-DP2 [25] (PDB ID: 3LQZ), which involves mostly hydrophobic interactions with only one hydrogen bond (Fig. 2b). A unique feature of the HLA-DP5•Cry j 1 peptide interactions is that the side chain of one of the anchoring residues, Lys(p1), hydrogen bonds with Gln31α and Asp84β (Fig. 2d). The main chain, but not the side chain, of Val(p2) hydrogen bonds with Tyr9α and Asn80β (Fig. 2d). On the other hand, the side chain of Thr(p3) forms hydrophobic interactions with Phe22α and Phe54α (Fig. 2e). The side chain of Val(p4) also forms hydrophobic interactions with Phe24β, Val72β, and Met76β, while the main chain hydrogen bonds with Asn62α and Gln13β (Fig. 2e). The main chain of Ala(p5) hydrogen bonds with Lys69β (Fig. 2e). The side chain of another anchoring residue, Phe(p6), interacts hydrophobically with Met11α, Leu66α, and Tyr26β (Fig. 2e). The side and main chains of Asn(p7) hydrogen bond with Tyr28β and Asn69α, respectively (Fig. 2f). The side chain of Gln(p8) hydrogen bonds with Asn68α (Fig. 2f). Finally, the side chain of Phe(p9) forms hydrophobic interactions with Leu73α, Phe9β, Leu35β, Val36β, and Trp59β (Fig. 2f). In addition, the side chains of Val(p2), Thr(p3), and Val(p4) do not fill their corresponding pockets, indicating that some larger side chains might be accommodated in these pockets (Fig. 2c).

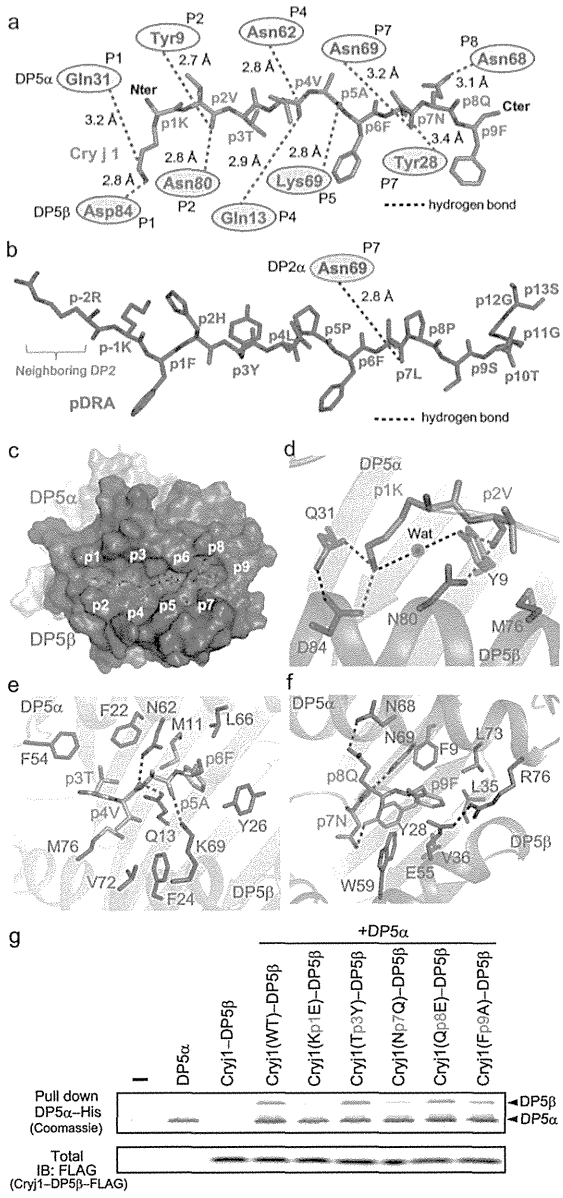

Fig. 2. Binding mode of the HLA-DP5•Cry j 1(9-mer) complex. (a) The hydrogen bonds between HLA-DP5 and the Cry j 1(9-mer) peptide. The residues of HLA-DP5α and HLA-DP5β involved in direct hydrogen bonding are labeled in green and blue circles, respectively. The Cry j 1(9-mer) peptide is shown as an orange stick model. (b) The hydrogen bond between HLA-DP2 and the pDRA peptide (PDB ID: 3LQZ). The pDRA peptide is shown as a purple stick model. The residue of HLA-DP2α involved in direct hydrogen bonding is labeled in the purple circle. (c) Top view of the Cry j 1(9-mer) peptide and the nine pockets in the peptide-binding groove. HLA-DP5α and HLA-DP5β are shown in green and blue surface presentations, respectively. The Cry j 1(9-mer) peptide is depicted by an orange stick model. Details of the Cry j 1(p1–p2) (d), Cry j 1(p3–p6) (e), and Cry j 1(p7–p9) (f) interactions in the peptide-binding groove of HLA-DP5 are shown. (a–e) The hydrogen bonds are represented as broken lines. (g) Mutant analysis based on the HLA-DP5•Cry j 1(9-mer) complex. HLA-DP5 was prepared by co-expressing HLA-DP5α and the Cry j 1–HLA-DP5β fusion protein in the cell-free synthesis system. Interactions of the Cry j 1(9-mer) mutants with HLA-DP5 were analyzed: His-tagged HLA-DP5α was captured and stained with Coomassie Brilliant Blue (top panel), and FLAG-tagged Cry j 1–HLA-DP5β was immunoprecipitated and detected by Western blotting (bottom panel). Representative data from three independent experiments are presented.

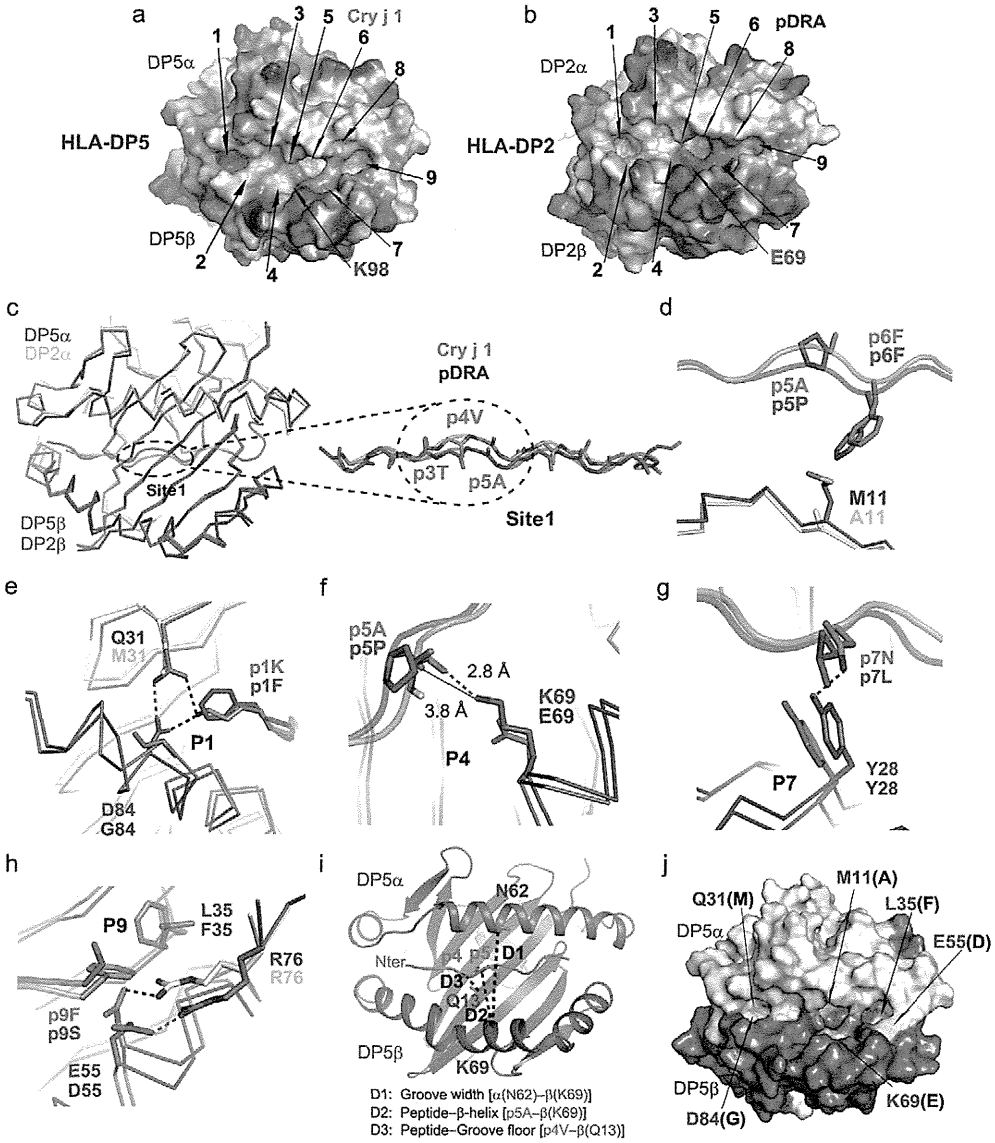

Fig. 3. Comparison of the HLA-DP5•Cry j 1(9-mer) complex with the HLA-DP2•pDRA complex. (a and b) Electrostatic potential maps of HLA-DP5 (a) and HLA-DP2 (b). Positive potential, blue; negative potential, red. The positions of the P1–P9 pockets for the Cry j 1 and pDRA peptides are indicated. (c) Superimposition of the HLA-DP5•Cry j 1(9-mer) complex on the HLA-DP2•pDRA complex. The major structural difference in the backbones of the peptides is indicated with a broken circle (Site 1). (d–h) Close-up views in stick presentations. Details of the Site 1 (d) and P1 (e), P4 (f), P7 (g), and P9 (h) pockets are shown. (c–h) The peptides and HLA molecules are colored orange (Cry j 1), purple (pDRA), green (HLA-DP5α), blue (HLA-DP5β), white (HLA-DP2α), and gray (HLA-DP2β), respectively. (i) According to Ref. [25], we compared the published human and mouse major histocompatibility complex II structures with a bound peptide with the total width of the peptide-binding groove (D1), the size of the gap between the peptide and the β chain α helix (D2), and the distance between the peptide and the floor of the binding groove (D3). (j) Non-conserved residues of the peptide-binding grooves between HLA-DP5 and HLA-DP2 are shown in yellow. The residues of HLA-DP5α and HLA-DP5β are labeled in green and blue, respectively, and those of HLA-DP2 are shown in parentheses.

To examine the contributions of the Cry j 1 side chains to the binding with HLA-DP5α and/or HLA-DP5β, we created five mutants of the Cry j 1 9-mer peptide (Fig. 2g). In this study, HLA-DP5 was prepared by co-expressing HLA-DP5α and the Cry j 1–HLA-DP5β fusion protein in the cell-free synthesis system, since the HLA-DP5α•HLA-DP5β heterodimer was not formed by the co-expression of HLA-DP5α and HLA-DP5β without the Cry j 1 fusion. Using this property, we analyzed the interactions of the Cry j 1 9-mer mutants with HLA-DP5: His-tagged HLA-DP5α was captured, and the level of HLA-DP5α•Cry j 1–HLA-DP5β complex formation was monitored by the amount of co-precipitated Cry j 1–

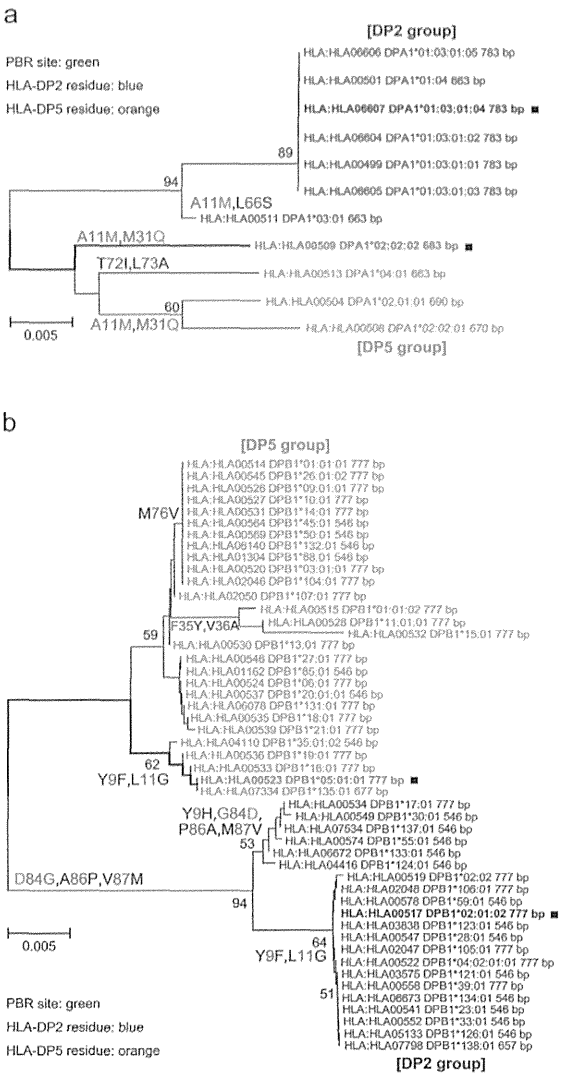

Fig. 4. Phylogenetic analyses of the HLA-DP alleles. (a) Phylogenetic tree of the HLA-DPA1 alleles. (b) Phylogenetic tree of the HLA-DPB1 alleles. (a and b) The NJ tree was constructed with only synonymous substitutions. Only the amino acid substitutions that occurred in the PBR were parsimoniously inferred and placed on or under each branch. For simplicity, not all amino acid substitutions on the main branches are shown. Particularly, position 55, 65, or 69 of the DPβ chain is not listed in each branch because of high-frequency replacement. For DPA1, the ancestral state was determined by a comparison with HLA-DRA. However, no appropriate outgroup sequence was found for DPB1, and the ancestral state was inferred from the extant sequences. Green characters represent substitutions in the PBR. Blue and orange characters indicate residues of HLA-DP2 and HLA-DP5, respectively.

HLA-DP5β. Mutations at the p1, p7, and p9 positions of the Cry j 1 peptide reduced the level of HLA-DP5α•HLA-DP5β complex formation (Fig. 2g). The effects of the p1 and p7 mutations were quite drastic. Lys(p1) is bound in the deep acidic pocket involving Gln31α and Asp84β, and its mutation to Glu (Kp1E) caused repulsion within the pocket (Fig. 2d). The mutation of Asn(p7) to the longer Gln (Np7Q) may have impaired the hydrogen bonding with Tyr28β (Fig. 2f). The mutation of Phe(p9) to Ala (Fp9A) probably weakened the hydrophobic interaction with the p9 pocket (Fig. 2f). In contrast, the Tp3Y and Np8E mutations exhibited negligible effects on the level of complex formation (Fig. 2g). Actually, the Tyr substitution for Thr(p3) may be accommodated well in the pocket constituted by Phe22α and Phe54α (Fig. 2e), while Glu at position p8 may interact with the pocket in the same manner as Gln(p8) (Fig. 2f).

Properties of the peptide-binding grooves of HLA-DPs and other class II HLA molecules

The HLA-DP5•Cry j 1 and HLA-DP2•pDRA complex structures superimposed on each other almost perfectly, with an rmsd value of 1.0 Å for the equivalent C_α atoms. In the HLA-DP5 and HLA-DP2 structures, the P1, P4, P6, and P9 pockets are significantly deeper than the P2, P3, and P7 pockets (Fig. 3a and b). However, each of the four deeper pockets of HLA-DP5 has a different position, size, or charge from that of the corresponding pocket of HLA-DP2. The bottom of the P1 pocket of HLA-DP5 consists of Gln31α and Asp84β and is negatively charged (Fig. 3a and e). Therefore, the HLA-DP5 P1 pocket is suitable for accommodating a positively charged amino acid residue, such as Lys. In contrast, the bottom of the HLA-DP2 P1 pocket is hydrophobic (Fig. 3b and e). The acidic P1 pocket is also present in some class II HLA structures, such as HLA-DQ2 [18], HLA-DQ2.3 [19], and HLA-DQ8 [20]. On the other hand, the P4 pocket of HLA-DP5 has a positive charge (Lys69β), whereas that of HLA-DP2 has three negative charges (Glu26β, Glu68β, and Glu69β) (Fig. 3a and b) [25]. The distance between the P6 and P9 pockets of HLA-DP5 is shorter than that of HLA-DP2 (Fig. 3a and b); the Tyr28β side chain shifts toward the P9 pocket and hydrogen bonds with Asn(p7)(Cry j 1) (Fig. 3g). Furthermore, the diameter and the depth of the P9 pocket are larger in HLA-DP5 than in HLA-DP2 [25] (Fig. 3a and b) due to the differences between Glu55β(HLA-DP5) and Asp55β(HLA-DP2) and between Leu35β(HLA-DP5) and Phe35β(HLA-DP2) (Fig. 3h).

We compared the width of the peptide-binding groove, represented by the distance between position 62α in the α1 domain and position 69β in the β1 domain (Fig. 3i) of HLA-DP5 with those of HLA-DP2 and other class II major histocompatibility complex/HLA molecules. The peptide-binding groove of HLA-DP2 is the widest (16.18 Å) [25]. By contrast, the groove width of HLA-DP5 is 15.08 Å, which is close to the average value (15.01 Å) [25] of the other structures. We also measured the distance between the peptide and the groove floor, as